



HAL
open science

The sulfur budget and sulfur isotopic composition of Martian regolith breccia NWA 7533

Jean-pierre Lorand, Jabrane Labidi, Claire Rollion-bard, Emilie Thomassot,
Jeremy Bellucci, Martin Whitehouse, Alexander Nemchin, Munir Humayun,
James Farquhar, Roger Hewins, et al.

► **To cite this version:**

Jean-pierre Lorand, Jabrane Labidi, Claire Rollion-bard, Emilie Thomassot, Jeremy Bellucci, et al..
The sulfur budget and sulfur isotopic composition of Martian regolith breccia NWA 7533. *Meteoritics
and Planetary Science*, 2020, 55, pp.2097-2116. 10.1111/maps.13564 . hal-02955751v2

HAL Id: hal-02955751

<https://hal.science/hal-02955751v2>

Submitted on 17 Sep 2024

HAL is a multi-disciplinary open access archive for the deposit and dissemination of scientific research documents, whether they are published or not. The documents may come from teaching and research institutions in France or abroad, or from public or private research centers.

L'archive ouverte pluridisciplinaire **HAL**, est destinée au dépôt et à la diffusion de documents scientifiques de niveau recherche, publiés ou non, émanant des établissements d'enseignement et de recherche français ou étrangers, des laboratoires publics ou privés.

1
2
3
4 1
5
6 2
7
8 3
9
10 4
11
12 5 **THE SULFUR BUDGET AND SULFUR ISOTOPIC COMPOSITION OF MARTIAN**
13 6 **REGOLITH BRECCIA NWA 7533**
14
15 7
16
17 8
18
19 9
20
21 10
22

23 11 Jean-Pierre LORAND¹, Jabrane LABIDI^{2,3,4}, Claire ROLLION-BARD⁴, Emilie THOMASSOT⁵, Jeremy J.
24 12 BELLUCCI⁶, Martin WHITEHOUSE⁷, Alexander NEMCHIN⁶, Munir HUMAYUN⁸, James FARQUHAR³, Roger
25 13 H. HEWINS^{9,10}, Brigitte ZANDA⁹, Sylvain PONT⁹
26

27 14 ¹Laboratoire de Planétologie et Géodynamique à Nantes, CNRS UMR 6112, Université de Nantes, 2 Rue de la
28 15 Houssinière, BP 92208, 44322 Nantes Cédex 3, France. (jean-pierre.lorand@univ-nantes.fr)
29 16

30 17 ²Geophysical Laboratory, Carnegie Institution of Washington, Washington, D.C. 20015, USA
31 18 (jlabidi@carnegiescience.edu)
32

33 19 ³Department of Geology, University of Maryland, College Park MD, 20740, USA
34

35 20 ⁴Université de Paris, Institut de physique du globe de Paris, CNRS, F-75005 Paris, France (rollion@ipgp.fr)
36

37 21 ⁵CRPG-CNRS, Nancy, France (emilie.@cprg.cnrs-nancy.fr);
38

39 22 ⁶Dept. of Applied Geology, Curtin University, Perth, WA 6845, Australia (jeremy.belluci@gmail.com; A.
40 23 Nemchin@curtin.edu.au);
41

42 24 ⁷Laboratory for Isotope Geology, Swedish Mus. of Nat History, Stockholm SE-104 05, Sweden
43 25 (martin.whitehouse@nrm.se)
44

45 26 ⁸Department of Earth, Ocean & Atmospheric Science and National High Magnetic Field Laboratory, Florida State
46 27 University, Tallahassee, FL 32310, USA (humayun@magnet.fsu.edu)
47

48 28 ⁹Institut de Minéralogie, de Physique des Matériaux, et de Cosmochimie (IMPMC) - Sorbonne Université- Muséum
49 29 National d'Histoire Naturelle, UPMC Université Paris 06, UMR CNRS 7590, IRD UMR 206, 61 rue Buffon, 75005
50 30 Paris, France.(hewins@rci.rutgers.edu; zanda@mnhn.fr ; spont@mnhn.fr)
51

52 31 ¹⁰Department of Earth & Planetary Sciences, Rutgers University, Piscataway, NJ 08854, USA
53 32
54

55 33 *Corresponding author : jean-pierre.lorand@univ-nantes.fr*
56
57
58
59
60

1
2
3 34 Abstract. The sulfur isotope budget of Martian regolith breccia (NWA 7533) has been addressed
4
5 35 from conventional fluorination bulk-rock analyses and ion microprobe in-situ analyses. The bulk
6
7 36 rock analyses yield 865 ± 50 ppm S in agreement with LA-ICP-MS analyses. These new data
8
9 37 support previous estimates of 80% S loss resulting from terrestrial weathering of NWA 7533
10
11 38 pyrite. Pyrite is by far the major S host. Apatite and Fe oxyhydroxides are negligible S carriers,
12
13 39 as are the few tiny igneous pyrrhotite-pentlandite sulfide grains included in lithic clasts so far
14
15 40 identified. A small non-zero $\Delta^{33}\text{S}$ (-0.029 ± 0.010 ‰) signal is clearly resolved at the 2σ level in
16
17 41 the bulk-rock analyses, coupled with negative CDT-normalized $\delta^{34}\text{S}$ (-2.54 ± 0.10 ‰), and near
18
19 42 zero $\Delta^{36}\text{S}$ (0.002 ± 0.09 ‰). In-situ analyses also yield negative $\Delta^{33}\text{S}$ values (-0.05 to -0.30 ‰)
20
21 43 with only a few positive $\Delta^{33}\text{S}$ up to $+0.38$ ‰. The slight discrepancy compared to the bulk-rock
22
23 44 results is attributed to a possible sampling bias. The occurrence of mass-independent
24
25 45 fractionation (MIF) supports a model of NWA 7533 pyrite formation from surface sulfur that
26
27 46 experienced photochemical reaction(s). The driving force that recycled crustal S in NWA 7533
28
29 47 lithologies—magmatic intrusions or impact-induced heat—is presently unclear. However, in-situ
30
31 48 analyses also gave negative $\delta^{34}\text{S}$ values ($+1$ to -5.8 ‰). Such negative values in the hydrothermal
32
33 49 setting of NWA 7533 are reflective of hydrothermal sulfides precipitated from $\text{H}_2\text{S}/\text{HS}^-$ aqueous
34
35 50 fluid produced via open-system thermochemical reduction (TSR) of sulfates at high temperatures
36
37 51 ($>300^\circ\text{C}$).
38
39 52

53 INTRODUCTION

54
55 In the absence of ozone, terrestrial sulfur of Archean age exhibits prominent mass
56
57 56 independent isotope fractionation (MIF) effects due to UV irradiation of atmospheric SO_2 to
58
59 57 form a variety of reduced and oxidized sulfur species (Farquhar et al., 1998; Pavlov and Kasting,
60
61 58 2002; Farquhar et al., 2002). The martian atmosphere is likely to have had similar UV irradiation
62
63 59 effects on volcanically produced SO_2 over most of martian history, thus producing mass-
64
65 60 independent fractionation in S isotopic signatures (Farquhar et al., 2000; Halevy et al., 2007;
61
62 61 Righter et al., 2009). In contrast to Earth, the martian sulfur cycle may have been dominated
63
64 62 throughout its geochemical history by processes operating at the martian surface due to the lack
65
66 63 of an efficient sulfur crustal recycling mechanism (Foley et al., 2003; King and McLennan,
67
68 64 1990; Franz et al., 2019 and references therein). Landers, rovers, and remote sensing
69
70 65 observations by orbiting spacecraft using different spectrometers identified a great diversity of

1
2
3 66 Ca-, Mg-, Fe-sulfate minerals as major components of the martian surface (see a review in Franz
4 et al., 2019a). The abundance and diversity of sulfate minerals testify to a wide range of
5 67 formation processes such as sulfur output through volcanic outgassing of SO₂ (Gaillard et al.
6 68 2009; Tian et al. 2015; Kerber et al. 2015; Franz et al, 2017), oxidation or acid weathering of
7 69 pre-existing igneous pyrrhotite/pyrite to Fe-sulfates (e.g. Zolotov and Shock, 2005; Dehouck et
8 70 al., 2012), hydrothermal precipitation (e.g. McCubbin et al., 2009), and brines from low pH
9 71 waters that contained sulfuric acid (e.g. McLennan et al., 2005), to near neutral, low-salinity
10 72 water that precipitated Ca sulfates by evaporation (e.g. Grotzinger et al., 2013; Nachon et al.,
11 73 2014). The Curiosity rover has identified Ca-sulfate-bearing fractures of diagenetic origin
12 74 deposited from near neutral water in the fluvio-lacustrine sedimentary sequence filling the
13 75 Noachian Gale Crater (Grotzinger et al., 2013; Nachon et al., 2014). Thick veins of Ca-sulfate
14 76 (gypsum) were also identified at Endeavour crater by the Opportunity rover (Squyres et al.,
15 77 2012).
16 78

17 79 Sulfates of martian origin were also identified in the interior of martian meteorites. The
18 80 Chassigny meteorite shows Ca-sulfate associated with carbonate veins (Wentworth and Gooding
19 81 1994). Nakhlite meteorites show evaporitic Ca-sulfate (gypsum, anhydrite) associated with
20 82 halite, Fe-rich carbonate, saponite, Fe³⁺ oxides and silica gels, all well preserved in the Nakhla
21 83 meteorite (Gooding et al. 1991; Bridges and Grady, 2000). Jarosite was found in a melt inclusion
22 84 inside clinopyroxene in MIL 03346 nakhlite (McCubbin et al. 2009). These different sulfates
23 85 point to episodic periods of water flow that exchanged sulfur processed with the atmosphere and
24 86 then deposited oxidized sulfur-bearing minerals through fractures, millions of years after
25 87 complete solidification of the igneous mass (Changela and Bridges, 2011; Bridges et al., 2019,
26 88 and references therein). Sulfates were also assimilated into the nakhlite parent magma at the
27 89 igneous stage, as shown by isotopically anomalous igneous pyrrhotite (Franz et al., 2014; Dottin
28 90 et al., 2018; Mari et al., 2019) that reequilibrated its metal-to-sulfur ratios toward metal-deficient
29 91 compositions (Chevrier et al., 2011; Mari et al., 2019). The nakhlite meteorites which contain
30 92 both sulfate and magmatic sulfide minerals display the largest range of MIF anomalies (Farquhar
31 93 et al., 2007b; Franz et al., 2014 ; Dottin et al., 2018). The Lafayette meteorite, another nakhlite
32 94 contains sulfates and/or sulfides with positive $\Delta^{33}\text{S}$ anomalies (like the Chassigny meteorite)
33 95 while Fe sulfides from the 4.1 Ga-old orthopyroxenite ALH 84001 display large variations from
34 96 negative to positive $\Delta^{33}\text{S}$ values ($-1.10 \pm 0.14\text{‰}$ to $0.66 \pm 0.22\text{‰}$) (Farquhar et al., 2000b; Franz
35
36
37
38
39
40
41
42
43
44
45
46
47
48
49
50
51
52
53
54
55
56
57
58
59
60

1
2
3 97 et al., 2014).

4
5
6 98 Sulfur isotope exchange between oxidized and reduced forms of sulfur during
7
8 99 hydrothermal circulation can also generate large mass-dependent fractionations of S isotopes.
9
10 100 Impact-driven hydrothermal activity is thought to explain $\delta^{34}\text{S}$ of -9 to -10 ‰ in carbonate-
11
12 101 associated pyrites of the 4.1 Ga-old orthopyroxenite ALH 84001 (Shearer et al., 1996). Franz et
13
14 102 al (2017) documented Fe-sulfides strongly depleted in ^{34}S ($\delta^{34}\text{S} = -47 \pm 14\%$) in the Cumberland
15
16 103 (CB) and Oudam (OU) fluvio-lacustrine sediments of Gale Crater. These values were interpreted
17
18 104 to be produced by equilibrium isotopic fractionation between sulfides and sulfates in
19
20 105 groundwater warmed by impact or igneous intrusions (Franz et al., 2017). Regolith breccia
21
22 106 NWA 7533 (paired with the so-called “Black Beauty” meteorite NWA 7034 (Agee et al., 2013)
23
24 107 and paired stones) that has sampled 4.4 Ga old impact lithologies (Humayun et al., 2013) is of
25
26 108 special interest for testing this suggestion of Franz et al. (2017). Unlike SNC meteorites, regolith
27
28 109 breccias are almost devoid of magmatic sulfides and contain sulfides of mostly hydrothermal
29
30 110 origin (pyrite and scarce pyrrhotite; Lorand et al., 2015). This Ni-rich (up to 4.5 wt.% Ni) pyrite
31
32 111 is primary unlike other hydrothermal pyrite occurrences so far reported in SNC meteorites and
33
34 112 ALH 84001 that are instead the oxidation product of more reduced sulfides (Shearer et al, 1996;
35
36 113 Greenwood et al., 2000; Lorand et al., 2018a). This pyrite likely reflects S-rich hydrothermal
37
38 114 fluids that percolated through the breccia billions of years after breccia formation (Lorand et al.,
39
40 115 2015; Goderis et al., 2016).

41
42 116 Our aim is to address the origin of S in the late circulating fluids using the S budget from
43
44 117 both bulk-rock S contents and S multi-isotope systematics. We focus on NWA 7533 because it is
45
46 118 the only one among the impact breccia samples that has been studied in detail for pyrite
47
48 119 distribution and composition including chalcophile trace elements (Lorand et al., 2015; 2018b).
49
50 120 The sulfur isotope analyses were done both with digestion of powdered rocks and by ion
51
52 121 microprobe *in-situ* measurements on pyrite and pyrrhotite. These data are used to build a
53
54 122 comprehensive picture of hydrothermal S cycling in this polymict regolith breccia.
55
56 123

51 124 **MAIN PETROGRAPHIC FEATURES OF NWA 7533**

52 125

53 126 The petrogenesis of NWA 7533 impact breccia has been reported in a series of recent
54
55 127 papers (Wittmann et al., 2015; McCubbin et al., 2016; Hewins et al., 2017). Its impact origin was
56
57
58
59
60

1
2
3 128 identified from the rock textures (various lithic clasts and impact melt rocks) and high (up to
4 129 1,000 ppm Ni, $1 < \text{Ir} < 100$ ppb) concentrations of siderophile elements (Ni, Ir and other highly
5 130 siderophile elements - HSE) (Humayun et al., 2013; Wittmann et al., 2015; Goderis et al., 2016).
6
7 131 NWA 7533 meteorite was classified as a polymict breccia because it is composed of separate
8
9 132 clasts with chemical compositions that require multiple igneous, sedimentary or impact-melt
10
11 133 sources (see Hewins et al., 2017, and references therein).

12
13
14 134 Briefly, its fine-grained Inter-Clast matrix (ICM) contains lithic clasts (norite,
15 135 monzonite) and single mineral clasts derived from these rocks and probably orthopyroxenite, as
16
17 136 well as clast-laden melt rocks (CLMR), microbasalt, and melt spherules. Noritic clasts are
18
19 137 composed of ferroan pyroxene ($\text{En}_{<72}$), orthopyroxene or inverted pigeonite, plagioclase (An_{50-30})
20 138 and Cr-rich magnetite. Monzonitic clasts show alkali feldspar, often perthitic, associated with
21
22 139 plagioclase ($<\text{An}_{30}$), ferroan pyroxene, chlorapatite and Fe-Ti oxides (magnetite, ilmenite and
23
24 140 accessory rutile). Noritic and monzonitic clasts contain zircon and baddeleyite that may also
25
26 141 occur as individual mineral clasts. Zircons in NWA 7533 and paired meteorites yielded pre-
27
28 142 Noachian, U-Pb crystallization ages of 4.47-4.35 Ga with a discordance implying a disturbance
29
30 143 at around 1.4 Ga (Humayun et al., 2013; Bellucci et al., 2015; McCubbin et al., 2016; Bouvier et
31
32 144 al., 2018). Crystal clasts are fragments of disaggregated lithic clasts. Noritic and monzonitic
33
34 145 clasts show widespread evidence of impactor-derived contamination: their concentration levels
35
36 146 of siderophile elements (Ni, Ir...) indicate that 3-5 % impactor materials accumulated over
37
38 147 repeated impact events (Humayun et al., 2013). This pervasive siderophile enrichment in the
39
40 148 melt rocks suggests a thick sequence of impact-generated rocks including mature regolith. The
41
42 149 monzonite clasts were formed by either differentiation of these large impact melt sheets or re-
43
44 150 melting of primary martian crust at depth in the presence of volatiles. A few pyroxene clasts
45
46 151 contain exsolution implying prolonged cooling at depth. Another zoned pyroxene population
47
48 152 suggests near surface crystallization (Leroux et al., 2016; Hewins et al., 2017 and references
49
50 153 therein).

51
52 154 Microbasalts and CLMR clasts show closely similar bulk composition and similar
53
54 155 siderophile element enrichment (Humayun et al., 2013). CLMRs are composed of plagioclase
55
56 156 laths and subophitic pyroxene indicating rapid quenching due to incorporation of abundant
57
58 157 clasts. Microbasalts are composed of orthopyroxene (En_{73-63}) or pigeonite (En_{63-49}), augite (En_{46-}
59
60 158 29), plagioclase (An_{66-30}) and Fe-rich spinel. Because of their subophitic to granoblastic textures,

1
2
3 159 microbasalts are interpreted as impact melt that crystallized less rapidly than CLMR (Hewins et
4 160 al., 2017). Regarding lithophile trace element geochemistry, the spherules, the groundmass of the
5 161 melt rock and the microbasalts resemble melted wind-blown dust and regolith debris (Humayun
6 162 et al., 2013). The dense ICM consists of anhedral micrometer-sized plagioclase embedded in
7 163 sub-micrometer sized pyroxene, plus fine-grained Fe-(Ti) oxides – magnetite and maghemite
8 164 (Muttik et al., 2014; Leroux et al., 2016). Disturbances in several isotopic systems (U-Pb in
9 165 zircon; K-Ar/Ar-Ar; Pb-Pb in phosphates; bulk-rock Re/Os systematics) indicate a probable
10 166 major reheating event that annealed the breccia at 1.35–1.4 Ga (Humayun et al., 2013;
11 167 McCubbin et al., 2016; Bellucci et al., 2015; Goderis et al., 2016; Hewins et al., 2017; Cassata et
12 168 al., 2018; see also Leroux et al., 2016).

170 **SULFIDE MINERALOGY OF NWA 7533**

171
172 The sulfide mineralogy in NWA 7533 impact breccia was previously studied from the
173 seven polished sections (7533-1 to -7) and one doubly polished transparent thick section (7533-
174 LM) available at the Museum National d'Histoire Naturelle (MNHN) (Lorand et al., 2015).
175 NWA 7533 is unique among martian meteorites in being almost devoid of the magmatic sulfide
176 assemblage of igneous origin (i.e. pyrrhotite-pentlandite-chalcopyrite) repeatedly reported in
177 SNC meteorites (e.g. Chevrier et al., 2011; Lorand et al., 2005; 2018a; Baumgartner et al., 2017;
178 Franz et al., 2014; 2019a,b; Dottin et al., 2018; Mari et al., 2019). Ni-bearing pyrrhotite (3 wt%
179 Ni) + pentlandite; was identified only as three inclusions in plagioclase clasts over the eight
180 polished thick sections investigated. By contrast, accessory pyrite (0.6-1% by weight according
181 to an X-Ray distribution map of S and point counting estimates) is widespread and evenly
182 distributed in all of the impact lithologies (monzonitic and noritic clasts, clast-laden melt rocks
183 (CLMR), melt spherules and microbasalts), in orthopyroxenite clasts from the pristine martian
184 crust, as well as in ICM and the late veins cutting across the meteorite. Hence, pyrite is a late-
185 stage mineral that crystallized after the final assembly of the breccia, during the annealing and
186 lithification event presumed to have occurred 1.4 Ga ago (Lorand et al., 2015).

187 Pyrite crystals show combinations of cubes, truncated cubes and octahedra (average grain
188 size 30-40 μm). These euhedral crystals were observed mostly inside open cracks, microbasalts
189 and ICM (Fig. 1A). In addition to occurring as euhedral crystals, many pyrites are anhedral

1
2
3 190 grains, sometimes of very small size (down to 1 μm across), especially when disseminated inside
4
5 191 ICM (Fig. 1B). Some anhedral pyrite grains replace low-Ca pyroxene clasts. Whether euhedral
6
7 192 or anhedral, many pyrite grains are poikiloblastic and enclose relict micron-sized Fe-(Ti) oxides
8
9 193 identified as being the same composition and habit as the magnetite-maghemite that is so
10
11 194 abundant in NWA 7533 (Fig. 1B). Pyrite-producing reactions thus involved sulfidation, either
12
13 195 from magnetite/maghemite, from the low-Ca pyroxene, or from dissolved divalent iron in a fluid.
14
15 196 Regardless of their mode of formation, NWA 7533 pyrite grains show nickel-rich areas (up to
16
17 197 4.5 wt.%; EMPA and SEM data) representing former Fe-Ni metal particles, as well as highly
18
19 198 siderophile element-rich micro-inclusions (Os, Ir, Ru, Pt, Pd, Re, Mo) interpreted as altered
20
21 199 impactor debris of the pre-Noachian meteoritic bombardment (Lorand et al., 2015, 2018b). It
22
23 200 was inferred from this maximum Ni content (positively correlated with Se) that pyrite started
24
25 201 crystallizing at 400-500°C. Compared to pyrite, hydrothermal pyrrhotite is very scarce, always
26
27 202 anhedral, and highly spongy (see Fig 1C). The assemblage pyrite-pyrrhotite-magnetite and
28
29 203 maghemite defines Eh-pH conditions of hydrothermal fluids as near neutral H_2S -HS-rich
30
31 204 ($6 < \text{pH} < 10$) oxidizing fluids (minimum $\log f_{\text{O}_2}$ of $> \text{FMQ} + 2$ log units; Lorand et al., 2015) in
32
33 205 agreement with the redox conditions deduced from pyroxene clast decomposition into Mg-
34
35 206 rich pyroxene, silica, and Fe-oxide (Leroux et al., 2016). Hydrothermal alteration under
36
37 207 oxidizing conditions appears to have given rise to fine-grained Fe-rich phases
38
39 208 influencing the magnetic properties of the breccia (Gattaceca et al., 2014).

37 209 Pyrite, a very fragile mineral, shows planar fractures (Fig. 1) resembling planar
38
39 210 deformation features (PDF). The shock creating such planar fractures was a very late event,
40
41 211 because pyrite was one of the last phases to crystallize in the breccia on Mars (Lorand et al.,
42
43 212 2015). The fractures were possibly related to the excavation event that liberated the meteorite
44
45 213 from the martian subsurface crust, yet its shock intensity could not be determined due to the lack
46
47 214 of olivine and quartz (Hewins et al., 2017). These fractures acted as preferential pathways for
48
49 215 partial replacement of pyrite by iron oxyhydroxides of terrestrial origin according to their D/H
50
51 216 values and their distribution defining an alteration gradient throughout the meteorite (Lorand et
52
53 217 al., 2015). Electron Microprobe analyses (EMP) of altered and hydrated regions in pyrite show
54
55 218 compositions similar to that of goethite, but containing $\sim 4\%$ SiO_2 while electron diffraction data

1
2
3 219 indicate the presence of hematite, as well. These oxide mixtures will be treated as iron
4
5 220 oxyhydroxides in the present paper (see Table S20 in Hewins et al., 2017).

6 221
7
8 222 **ANALYTICAL METHODS**
9 223
10 224

11 225 The bulk analyses of the meteorite were performed on two powder splits (BB UMD 1 and
12 226 BB UMD 2) of 0.6 grams each. Both replicates yielded very similar results in terms of S contents
13
14 227 and S isotopic compositions (see below), so we assume that these powder splits were
15
16 228 representative of the entire breccia. Bulk sulfur abundances and sulfur isotopic compositions of
17
18 229 the bulk sulfur fractions were obtained at the University of Maryland, according to a technique
19
20 230 described in detail in Labidi et al. (2012). Briefly, powdered samples were digested in Teflon
21
22 231 vessels while continuously flushed with pure N₂. Twenty milliliters (ml) of 2.1 M CrCl₂ solution
23
24 232 and 5 ml of 29 N HF (48%, ultrapure) were used to digest the samples. The H₂S released in this
25
26 233 process was flushed to a sulfide trap filled with AgNO₃ solution (0.3 M) where it reacted to
27
28 234 precipitate Ag₂S. After each extraction and for all samples, weighed Ag₂S precipitate is
29
30 235 compared to the S content obtained with EMP and used to determine extraction yields. Weighed
31
32 236 silver sulfide samples were subsequently wrapped in Al-foil and placed in Ni reaction vessels for
33
34 237 fluorination with at least 10 times excess of pure F₂ at 250 °C overnight. The SF₆ produced was
35
36 238 isolated from impurities using cryogenic and chromatographic techniques. The volume of
37
38 239 purified SF₆ was then measured with a manometer and transferred to the dual inlet of a
39
40 240 ThermoFinnigan MAT 253 isotope ratio gas-source mass spectrometer that was used to measure
41
42 241 ion beams at m/z = 127+, 128+, 129+ and 131+. Once δⁿS values are determined (n = 33, 34,
43
44 242 36), Δ³³S and Δ³⁶S are calculated ($\Delta^{33}\text{S} = \delta^{33}\text{S} - 1000((\delta^{34}\text{S}/1000 + 1)^{0.515} - 1)$ and $\Delta^{36}\text{S} = \delta^{36}\text{S} -$
45
46 243 $1000((\delta^{34}\text{S}/1000 + 1)^{1.90} - 1)$). IAEA S1 values are used to evaluate our long-term accuracy and
47
48 244 precision on standards, and to anchor our δ³⁴S to the V-CDT scale. Analyses of the S1 standard
49
50 245 performed along with the Mars rock analyses yield average δ³⁴S, Δ³³S and Δ³⁶S values of -
51
52 246 5.28±0.09‰, +0.083±0.008‰ and -0.78±0.26‰ (n=13, all 2s.d.) relative to our reference gas
53
54 247 (see details in Labidi et al. 2017). Relative to the same reference gas, our CDT yield δ³⁴S, Δ³³S
55
56 248 and Δ³⁶S values at -4.88±0.15‰, -0.035±0.008‰ and -0.08±0.08‰ (n=6, all 2 s.d.). The S
57
58 249 isotope shift for δ³⁴S, Δ³³S and Δ³⁶S between CDT and S1 is comparable to what was obtained
59
60 250 elsewhere (Ono et al., 2006; Labidi et al., 2012). We use the CDT scale to anchor our δ³⁴S, Δ³³S

1
2
3 251 and $\Delta^{36}\text{S}$ values. We additionally report our $\delta^{34}\text{S}$ values on the V-CDT scale to allow
4
5 252 comparisons with other datasets that also reported $\delta^{34}\text{S}$ values relative to V-CDT (e.g., terrestrial
6
7 253 mantle-derived rocks, Labidi et al. 2012). We obtained 2σ uncertainties of 0.10, 0.012 and
8
9 254 0.25‰ for $\delta^{34}\text{S}$, $\Delta^{33}\text{S}$ and $\Delta^{36}\text{S}$ values, respectively, for all measurements with a SF_6 amount > 1
10
11 255 μmol .

12 256 The *in-situ* analyses of S multi-isotopes were done with ion probes on two polished thin
13
14 257 sections (7533-4 and 7533-5) over the 8 available. These two polished thin sections show
15
16 258 unaltered pyrite crystal cores large enough to be analysed. The dimensions and localisation of the
17
18 259 final ion microprobe spots were checked with a scanning electron microscope (Tescan VEGA II
19
20 260 LSU Scanning Electron Microscope (SEM) operating in conventional (high-vacuum) mode, and
21
22 261 equipped with an SD3 (Bruker) EDS detector (Muséum National d'Histoire Naturelle Paris,
23
24 262 France = MNHN) operating in the backscattered mode (BSE) (see Lorand et al., 2015 for more
25
26 263 details). Major element compositions of pyrite (Fe, Ni, S) were determined with the same
27
28 264 standard-less Energy Dispersive procedure as in Lorand et al. (2015) inside the ion beam craters
29
30 265 of SIMS analysis; these latter analyses agree quite well with pyrite compositions reported in
31
32 266 Lorand et al. (2015; 2018b)

31 267 Two Cameca IMS 1280 facilities (CRPG, Nancy, France; NordSIMS facility, Stockholm,
32
33 268 Sweden) (Table 1) were used. The analytical method for the CRPG Cameca IMS 1280 HR2 is
34
35 269 described in detail in Thomassot et al. (2009) and in Muller et al. (2016). Sulfur isotope
36
37 270 compositions of sulfides from thick section 7533-5 were measured by simultaneous
38
39 271 measurements of $^{32}\text{S}^-$, $^{33}\text{S}^-$, $^{34}\text{S}^-$, and $^{36}\text{S}^-$ in multicollection mode with three off-axis Faraday
40
41 272 cups (L'2, C and H1) that were intercalibrated before each session of analyses, and one electron
42
43 273 multiplier (H2) for the most rare isotope (^{36}S). The analytical settings were: 5 nA, Cs^+ - primary
44
45 274 beam focused to a spot of about 15 μm , with secondary intensities from 8.2×10^8 to 10.2×10^8
46
47 275 cps for ^{32}S , depending on the mineralogy. Gains and backgrounds of the Faraday cups were
48
49 276 regularly measured during the entire session. Measurements were performed with an automatic
50
51 277 centering process and consist of 30 cycles of 4 seconds each after a pre-sputtering time of 300
52
53 278 seconds. The background of the detectors was measured during the pre-sputtering and was then
54
55 279 used to correct each analysis. The internal precision achieved under these conditions was better
56
57 280 than 0.05‰ for $\delta^{34}\text{S}$ and 0.03‰ for $\delta^{33}\text{S}$ values (2σ). The external precision, determined from
58
59 281 repeated measurements on various reference materials, was 0.40‰ (2σ) for $\delta^{34}\text{S}$, 0.09‰ (2σ) for
60

1
2
3 282 $\Delta^{33}\text{S}$ values and 0.24‰ for $\Delta^{36}\text{S}$. Several pyrite in-house reference materials (Maine, Philippot et
4 al., 2012, Balmat pyrite, courtesy of M. Whitehouse, and Spain-CR, Muller et al., 2016) were
5 283 used to determine (i) the instrumental mass fractionation, and (ii) the reference mass
6 284 discrimination line, from which $\Delta^{33}\text{S}$ and $\Delta^{36}\text{S}$ values were calculated. The values of the in-house
7 285 reference materials can be found in Muller et al. (2017). The bulk isotopic compositions of these
8 286 materials were measured by conventional gas source mass spectrometer at IPGP following
9 287 Labidi et al. (2012).
10 288

11 289 Quadruple S-isotopes were measured in-situ on section 7533-4 at a ca. 10 μm scale using
12 290 a CAMECA ims1280 SIMS instrument (NordSIMS facility, Stockholm), closely following
13 291 analytical protocols outlined by Whitehouse (2013). The sulfur isotopes ^{32}S , ^{33}S and ^{34}S were
14 292 measured on Faraday detectors, while ^{36}S was measured on an ion counting electron multiplier,
15 293 corrected for drift using interspersed reference materials (Balmat and Ruttan pyrites), which
16 294 were also used to correct for instrumental mass bias. Isua pyrite was used to monitor the mass
17 295 independent values.
18 296

19 297 Sulfur contents of Fe oxyhydroxides and apatite that may be potential S reservoirs (e.g.
20 298 Parat et al., 2011) were analysed *in-situ* using a Laser Ablation Inductively Coupled Plasma
21 299 Mass Spectrometer (LA-ICP-MS) at the «Laboratoire de Planétologie et Géodynamique» in
22 300 Nantes (France) following the procedure described in detail by Lorand et al (2018b). The
23 301 samples were ablated and analysed for ^{34}S using a Bruker 880 quadrupole ICP-MS coupled with
24 302 a Photon Machine Analyte™ G2 equipped with an excimer laser (193 nm laser wavelength) and
25 303 a dual volume sample cell that keeps the sample volume small and constant. The laser was
26 304 operated with a repetition rate of 10 Hz and a laser output energy of 90 mJ with a 50% attenuator
27 305 and 20x demagnification, resulting in low fluences on the sample ($<4 \text{ J/m}^2$). Spot sizes for
28 306 standards and samples were set to 25-50 μm depending on the size of the mineral grains. Six Fe
29 307 oxyhydroxide grains replacing pyrite were analysed in section 7533-5 with a spot size of 25 μm ,
30 308 NIST 610 glass as calibration standard and SiO_2 content as internal standard, based on the values
31 309 published by Lorand et al. (2015) and Hewins et al. (2017). Eight apatite crystals from NWA
32 310 7533 - 5 were analysed with a laser spot size of 50 μm , NIST 612 glass as calibration standard
33 311 and Ca as internal standard based on the apatite analyses reported by Hewins et al. (2017).
34 312 Concentrations in both cases were determined using Glitter™ software (Table 2).
35
36
37
38
39
40
41
42
43
44
45
46
47
48
49
50
51
52
53
54
55
56
57
58
59
60

RESULTS

The two bulk-rock analyses yield quite reproducible bulk S concentrations (805-920 ppm). These bulk chemistry values are very close to the mean value calculated from LA-ICP-MS raster analyses of Humayun et al. (2013) although the latter method detected huge variations (100 to 1500 ppm) between each of the breccia components (CLIMR, ICM, microbasalts, melt spherules; see section 2), reflecting small scale variations in modal abundances and weathering degrees of pyrite (Lorand et al., 2015; 2018b). The samples yield an average $\Delta^{33}\text{S}$ of -0.029 ± 0.010 ‰ reflecting a small but resolvable non-zero signal in $\Delta^{33}\text{S}$ at the 2σ level. This non-zero $\Delta^{33}\text{S}$ is coupled with negative $\delta^{34}\text{S}$ (-2.54 ± 0.10 ‰). The NWA 7533 meteorite S isotopic composition is distinct from that of the juvenile martian S isotopic composition calculated by Franz et al. (2019) from 47 shergottite analyses ($\delta^{34}\text{S} = -0.24 \pm 0.05$ ‰, $\Delta^{33}\text{S} = 0.0015 \pm 0.0016$ ‰, $\Delta^{36}\text{S} = 0.039 \pm 0.054$ ‰).

In addition to bulk isotope measurements, 29 spot analyses were performed on 18 pyrite and 3 pyrrhotite grains of sufficient size (>20 μm) that were not significantly altered to Fe-oxyhydroxides. Ion microprobe measurements yielded more negative $\Delta^{33}\text{S}$ values ($-0.05 < \Delta^{33}\text{S} < -0.38$ ‰) compared to the bulk-rock analyses, and a wider range of negative $\delta^{34}\text{S}$ signatures ($-1.5 < \delta^{34}\text{S} < -3.1$ ‰; with outliers up to -5.5 and $+0.6$ ‰) (Fig. 2). The Nancy SIMS analyses show a larger scatter in the $\delta^{34}\text{S}$ and $\Delta^{33}\text{S}$ values than the bulk analyses and include two positive values for $\Delta^{33}\text{S}$ (0.24 - 0.35 ‰ corresponding to Site 16-1 and Site F-4 pyrites; Table 1). The ranges of $\Delta^{36}\text{S}$ are similar: -0.55 to $+0.49$ ‰ (NORDSIMS) vs. -0.9 to $+0.49$ ‰ (Nancy SIMS), excluding one outlier at -2.2 ‰ (**Site B-1** Pyrite). Correlation between $\Delta^{33}\text{S}$ and $\delta^{34}\text{S}$ is lacking (Fig. 2). There are no correlations between sulfur isotopic compositions and pyrite Ni contents (<0.1 - 3 wt.%; Table 1)(Fig. 3), suggesting that the correction procedure of SIMS analyses was not affected by the small deviation of NWA 7533 pyrite compared to pure FeS_2 . The spread in the $\delta^{34}\text{S}$ values seems to be due to beam overlap over polymineralic aggregates (pyrite-Fe oxides or Fe oxyhydroxides), matrix silicates or vein-filling terrestrial products (calcite). The analyses having incorporated some calcite seem to shift $\delta^{34}\text{S}$ toward more positive values (7533-5-19; 7533-5-17; 7533-5-F-2; 7533-5-1a) (Fig. 1). No systematic trend can be seen for those analyses overlapping Fe oxyhydroxides or matrix silicates ($\delta^{34}\text{S}$ down to -5.58 ‰ for NWA7533-5-G).

1
2
3 343 The six pyrite crystals analysed with the NORDSIMS ion microprobe show a very
4 similar range of negative $\Delta^{33}\text{S}$ values ($-0.05\text{‰} < \Delta^{33}\text{S} < -0.36\text{‰}$) to the 12 Nancy SIMS pyrite
5 344 analyses, however with no positive values. Both data sets also yield consistent results with
6 345 regard to the negative $\delta^{34}\text{S}$ value of NWA 7533 sulfides ($-3.3\text{‰} < \delta^{34}\text{S} < -1.5\text{‰}$). Duplicate
7 346 analyses generated variable reproducibility that reflected the different degrees of sulfide
8 347 alteration from one section to another (e.g. site 16a,b; Table 1), and the grain size of the
9 348 preserved pyrite. Pyrite and the three highly spongy pyrrhotite grains of hydrothermal origin
10 349 analysed here carry similar isotopic compositions at the 2-sigma level (Table 1; Fig. 2). Due to
11 350 their lower count rate the NordSIMS analyses of pyrrhotite are less precise compared to the
12 351 analyses of pyrite, as shown by the two sigma values of the three S isotope ratios. This lower
13 352 precision may result from the highly spongy nature of that pyrrhotite, showing pore sizes much
14 353 smaller ($< 1\text{ }\mu\text{m}$) than the ion beam diameter ($> 10\text{ }\mu\text{m}$).
15 354
16 355
17
18
19
20
21
22
23
24
25
26
27

28 356 DISCUSSION

29
30 357 At first sight, the occurrence of Mass Independent Fractionation of sulfur (S-MIFs)
31 supports a martian origin for sulfur in NWA 7533 as deduced from microtextural and
32 358 compositional characteristics of NWA 7533 pyrite (Lorand et al., 2015). Indeed, S-MIFs are
33 359 generated by UV-induced photochemical processes in an atmosphere poor in O_2 like the martian
34 360 atmosphere since the earliest times (e.g. Farquhar et al., 2000, 2001; Pavlov and Kasting, 2002).
35 361 In oxygen isotopes, MIF effects also affect the bulk-rock composition of NWA 7034 (Agee et
36 362 al., 2013), phosphates (Belluci et al., 2020) and are largest in NWA 7533 zircons (Nemchin et
37 363 al., 2014). Moreover, the variation in $\Delta^{33}\text{S}$ with an absence of significant anomalies in $\Delta^{36}\text{S}$ (Fig.
38 364 4) is considered to be diagnostic of S-MIF production on Mars, by different pathways from those
39 365 that operated on the early Earth and in Earth's stratosphere today (see e.g. Masterson et al.,
40 366 2011). The calculated mean $\Delta^{36}\text{S}$ value from both the bulk-rock and SIMS analyses is close to
41 367 0 ‰, a characteristic feature of S multi-isotope systematics of martian meteorites compared to
42 368 Archean terrestrial samples showing mass independent signatures (Franz et al., 2014,
43 369 2019a,b)(Fig. 4). The plot in Fig. 4 also rules out alternative fractionation processes, such as, for
44 370 example, mass-dependent fractionation during Rayleigh distillation with alternative mass laws
45 371
46
47
48
49
50
51
52
53
54
55
56
57
58
59
60

1
2
3 372 (e.g. Young et al., 2002). This latter process should produce a regression line characterized by a
4
5 373 slope of -7 ± 1 whereas our data set does not align on any correlation at all. However, it is worth
6
7 374 noting that all but three analyses of NWA 7533 sulfides plot within the scattergram of nakhlites
8
9 375 in the $\Delta^{36}\text{S}$ vs. $\Delta^{33}\text{S}$ plot of Fig. 4. This may be more than a coincidence because NWA 7533
10
11 376 sulfides were dated at 1.4 Ga, like nakhlites that recorded sulfate contamination at each stage of
12
13 377 their petrogenetic history (e.g. Franz et al., 2014; Dottin et al., 2018; Lindsay et al., submitted).
14
15 378 This could reflect the S isotopic composition of surficial sulfur at that time on the martian crust,
16
17 379 or a specific S reservoir sampled by both martian breccias and nakhlites.

17 380 The presence of sulfur isotopic variations that are both mass-independent and
18
19 381 mass-dependent compared to the inferred composition of martian mantle-derived
20
21 382 sulfur, argues in favor of a crustal origin of NWA 7533 pyrite consistent with its
22
23 383 hydrothermal origin (Lorand et al., 2015). Even taking into account only the bulk-rock
24
25 384 data, the small but significant negative $\Delta^{33}\text{S}$ values overlap with the isotopic S compositions
26
27 385 reported for some shergottites that are now considered to have assimilated crustal sulfur (NWA
28
29 386 11300; NWA 7635; Franz et al., 2019). Before further discussion, it is necessary to address any
30
31 387 bias in the database. Hence, the following three points will be addressed 1) how can the slight
32
33 388 discrepancy between in-situ analyses and bulk-rock determination of $\Delta^{33}\text{S}$ be explained, 2) how
34
35 389 was anomalous S transferred to impact breccias, and 3) what was the ultimate process that
36
37 390 triggered hydrothermal cycling of S in these martian regolith breccias.

37
38 391

39 392 **The balance of the bulk-rock S multi-isotope budget of NWA 7533**

40
41 393 Anomalous $\Delta^{33}\text{S}$ for pyrite was observed with two different ion microprobes in two
42
43 394 different laboratories. This argues for a significant negative $\Delta^{33}\text{S}$ anomaly as measured by SIMS,
44
45 395 which seems to conflict with the near-zero $\Delta^{33}\text{S}$ value of $-0.029\pm 0.010\%$ measured with precise
46
47 396 bulk S isotope measurements. It is not the first time that in-situ analyses and bulk-rock
48
49 397 determination of S isotopes do not match. Franz et al. (2014) documented quite a large
50
51 398 discrepancy between SIMS analyses and chemical extractions of MIL 03346 pyrrhotite ($\Delta^{33}\text{S} = -$
52
53 399 0.73 ± 0.13 vs. -0.43%) but did not propose a reason for the discrepancy. Dottin et al. (2018)
54
55 400 also reported SIMS analyses of nakhlites paired with MIL 00336 yielding lower $\Delta^{33}\text{S}$ compared
56
57 401 to bulk rocks, and argued that the SIMS measurements captured a different population of sulfides

1
2
3 402 than the bulk analyses. Another possible source of analytical bias is that S-bearing phases other
4 403 than the two Fe-sulfides, pyrrhotite and pyrite, were overlooked by petrographic studies.
5
6

7 404 Sulfur in NWA 7533 was identified as residing in both magmatic sulfide assemblages,
8 405 apatite and Fe-oxyhydroxides (Lorand et al., 2015; this study). As said before, the impact breccia
9 406 is almost devoid of magmatic sulfides, which is interpreted to result from repeated impact and
10 407 shock melting. It is well known that shock melts are strongly degassed (Pierazzo and Artemieva,
11 408 2012; Righter et al., 2015). Nickel, a strongly chalcophile element was demonstrated to behave
12 409 as a lithophile element in impact-melt derived noritic and monzonitic clasts that crystallized
13 410 without evolving sulfide melts (Hewins et al., 2017 and references therein). The paucity of
14 411 magmatic sulfides in NWA 7533 clearly reflects the repeated heavy bombardment of the martian
15 412 regolith. Another potential S carrier in igneous rocks is apatite (Parrat et al., 2011) which is a late
16 413 magmatic mineral in lithic clasts and microbasalts of the breccia (Hewins et al., 2017). NWA
17 414 7533 apatite S content determined by LA-ICP-MS is quite homogeneous (200-300 ppm; Table
18 415 2). However, apatite is a minor mineral (<6 vol% in NWA 7034, paired with NWA 7533; Agee
19 416 et al., 2013) and its contribution to the whole rock S budget is expected to be negligible (< 15
20 417 ppm vs. 865 ppm). Its effect on the S isotopic composition is difficult to predict without a
21 418 reliable apatite standard for SIMS isotope analyses. However, we can speculate that magmatic
22 419 sulfides or apatite containing juvenile martian sulfur would drive the S multi-isotope
23 420 composition of NWA 7533 toward 0 ‰ in the $\delta^{34}\text{S}$ vs. $\Delta^{33}\text{S}$ diagram of Fig. 2. Alternatively,
24 421 Humayun et al. (2014) suggested that NWA 7533 lithic clasts crystallized from impact
25 422 melts that incorporated already weathered clay-rich martian soils. In that case, evidence
26 423 from SNC meteorites and analyses of Gale crater sulfates (Greenwood et al., 2000;
27 424 Farquhar et al., 2007; Franz et al., 2014, 2017, 2019, Dottin et al., 2018; Mari et al., 2019)
28 425 predict deviation of $\delta^{34}\text{S}$ toward strongly positive values in Fig. 2. Clearly, neither
29 426 magmatic sulfides nor apatite could account for the dilution of the pre-existing non-zero $\Delta^{33}\text{S}$ at
30 427 near constant $\delta^{34}\text{S}$ between in-situ SIMS analyses and the two bulk-rock data.
31
32
33
34
35
36
37
38
39
40
41
42
43
44
45
46
47
48
49
50
51

52 428 Fe oxyhydroxides contain ten times more S than does apatite (3000±1000 ppm; now
53 429 measured *in-situ* with both EMP and LA-ICP-MS, Table 2). However, simple mass balance
54 430 calculations suggest that Fe oxyhydroxides are a negligible S reservoir, too. They would
55
56
57
58
59
60

1
2
3 431 represent c.a. 40 ppm S (5% of the bulk-rock S concentration) at best taking into account the
4
5 432 highest in-situ measured S content ($\approx 4,000$ ppm) and modal abundances of ca. 1 wt.% (implying
6
7 433 a total oxidation of pyrite, which is an over-estimate). Some of the sulfur of Fe oxyhydroxides
8
9 434 may come from both oxidized pyrites and terrestrial sources with near-zero $\Delta^{33}\text{S}$ values, which
10
11 435 would explain the shift in the bulk-rock $\Delta^{33}\text{S}$ values compared to ion microprobe data. From the
12
13 436 mass balance calculations, Fe oxyhydroxides would have to have unrealistically positive $\Delta^{33}\text{S}$ of
14
15 437 about +6 to +9 ‰ to explain the shift of $\Delta^{33}\text{S}$ from -0.2 ± 0.1 ‰ (SIMS data) relative to the
16
17 438 bulk value of -0.03 ± 0.01 ‰.

17 439 Sulfates, also major S-bearing phases on Mars (Franz et al., 2017, 2019 and reference
18
19 440 therein), have not been detected in martian breccia NWA 7533 despite careful SEM scanning of
20
21 441 the 8 polished pieces studied so far (Lorand et al., 2015; Hewins et al., 2017). There are no
22
23 442 coupled Ba+S spikes that could correspond to barite micro-inclusions in the time-resolved
24
25 443 diagram of the LA-ICP-MS analyses of Fe oxyhydroxides (Fig. 5). Barium was systematically
26
27 444 detected along with S (in agreement with EMP and TEM data for Ca, S and Si). The Sr and Ba
28
29 445 ion signals are highly correlated and the ^{34}S signal follows the Ba and Sr signals very closely in
30
31 446 the first portion of the scan in Fig. 5, while the Ca signal is independent of the Ba-Sr-S signals.
32
33 447 The high Sr might indicate that a Sr-Ba sulfate is the only sulfate present and that it is
34
35 448 sufficiently widely distributed at a nanometric scale in the Fe-oxyhydroxides not to form discrete
36
37 449 spikes. However, the trend of strongly decreasing S/Se ratio in NWA 7533 Fe oxyhydroxides
38
39 450 ($137 < \text{S/Se} < 1,193$) compared to their pyrite precursors ($3,500 < \text{S/Se} < 54,000$) supports the
40
41 451 hypothesis of extensive leaching of sulfates from the breccia during terrestrial weathering (Fig.
42
43 452 6). Such a drop in the S/Se ratios is consistent with the well documented differences in the
44
45 453 behaviour of S and Se in terrestrial weathering (e.g. Lorand et al., 2003 and ref. therein). Under
46
47 454 acidic conditions that characterize terrestrial weathering, both Se^{4+} and Se^{6+} tend to adsorb onto
48
49 455 naturally occurring Fe oxides and oxyhydroxides while S is leached as SO_4^{2-} (e.g. Ziemkiewicz et
50
51 456 al., 2011). From pyrite modal abundance (up to 1 wt.%; Lorand et al., 2015), NWA 7533 should
52
53 457 show a bulk-rock S content of 5,400 ppm S instead of 865 ± 80 ppm measured in the present
54
55 458 study. This suggests a loss of 80% S as dissolved sulfates during terrestrial weathering, which is
56
57 459 consistent with previous estimates, either based on pyrite/Fe oxyhydroxide modal ratios (Lorand
58
59 460 et al., 2015) or *in-situ* analyses of pyrite S and Se contents (Lorand et al., 2018b).

1
2
3 461 The discussion above casts serious doubt on whether another S reservoir with a
4 462 significant effect on bulk S isotopic composition is present in these breccias. Another possible
5 463 source of discrepancy between the bulk-rock analyses and in-situ measurements is analytical bias
6 464 generated by one or both of the two techniques. The bulk-rock analysis involved an extraction
7 465 procedure of S using a Cr(II) solution (c.f. Labidi et al., 2012) which has been shown to be very
8 466 inefficient for sulfates. (Gröger et al., 2009). However, this analytical bias was likely negligible
9 467 because as shown above, NWA 7533 meteorite lacks detectable amounts of sulfates. A
10 468 systematic analytical bias from both the Nancy and Stockholm SIMS can be ruled out because
11 469 multiple sulfur analyses were processed in both places the same way using the same reference
12 470 materials and both were mass resolved from $^{32}\text{S}^1\text{H}$. One may speculate that hydride generation
13 471 could be a bit higher on the sulfide standard mount block (in epoxy) (or if the standard sulfides
14 472 themselves are hydrated) than on the meteorite section, thus generating $\Delta^{33}\text{S}$ values biased
15 473 towards higher values that would in return make the unknowns lower in $\Delta^{33}\text{S}$. Another effect that
16 474 could alter the $\Delta^{33}\text{S}$ values measured by SIMS is the Faraday amplifier background drift. Many
17 475 of the sulfides analysed in our paper are yielding somewhat lower 70-80% count rates than the
18 476 standards so a small drift would have a disproportionate effect in any drift correction, probably at
19 477 around the 0.1 permil level (around 1000 cps in 10^7 cps), and it would lower $\Delta^{33}\text{S}$ too. However,
20 478 there is no direct evidence that this putative drift might have operated during the analytical
21 479 session of NWA 7533 sulfides. Moreover the background was systematically measured during
22 480 the pre-sputtering time.

23
24
25
26
27
28
29
30
31
32
33
34
35
36
37
38 481 The question that arises now is whether the SIMS analyses sampled one or several S
39 482 populations from the same sulfides (pyrite/and or pyrrhotite). This issue can be addressed by
40 483 looking at the uncertainty data on the average triple S compositions reported Table 1 as the
41 484 simple 2x standard deviation on the values, and the weighted average uncertainty on the data,
42 485 along with its MSWD value. Both the NORDSIMS and Nancy data set yield similar results :

43 486 □ large spread of data for $\delta^{34}\text{S}$ (MSWD of 42 for the NORDSIMS analyses and 132 for the
44 487 Nancy analyses), beyond what can be explained by analytical uncertainties. This scatter could
45 488 represent a real Mass Dependent Fractionation (MDF) trend or a subtle analytical issue. Hence,
46 489 the weighted average uncertainty is obviously not a useful measure of
47 490 the scatter for $\delta^{34}\text{S}$ that integrates a component of geological scatter (MDF).

491

1
2
3 492 -□ $\Delta^{33}\text{S}$ values define statistically single low MSWD (1.1 vs. 1.5 for the Nancy and NORDSIMS
4 data set, respectively) populations that are very slightly negative. In fact, combining both data
5 493 sets gives a weighted average of -0.165 ± 0.032 permil, not overlapping the bulk value. Of
6 494 course, the fact that $\delta^{34}\text{S}$ shows variation means that our analyses may have sampled two (or
7 495 more) reservoirs that are very slightly different in $\Delta^{33}\text{S}$. Testing that interpretation from a $\Delta^{33}\text{S}$
8 496 vs. $\delta^{34}\text{S}$ plot would demand many more analyses with much better individual data uncertainties
9 497 than we have. In that case, the calculation with standard deviations may apply, which would give
10 498 a mean $\Delta^{33}\text{S}$ value of -0.2 ± 0.18 (2SD) for the Stockholm data, -0.12 ± 0.22 (2SD) for the
11 499 Nancy data and a -0.16 ± 0.11 (2SD) for the combined
12 500 dataset. Taken individually, both mean $\Delta^{33}\text{S}$ values overlap the bulk rock data, but when
13 501 combined, they do not.
14 502

15 503 - Our $\Delta^{36}\text{S}$ averages are similar to each other and within error of the
16 504 bulk. However, the Nancy data display a greater spread (MSWD of 13) perhaps inconsistent with
17 505 sampling a single population.
18 506

19 507 To summarize, the fact that SIMS and bulk-rock data do not overlap at 95% confidence
20 508 suggests that the two techniques may have sampled different sulfur isotopic compositions from
21 509 the same Fe-sulfides, assuming that each data set (the UMD bulk-rock data, the NordSIMS data
22 510 and the Nancy data) are single populations. Thus, the case for multiple S populations could be
23 511 stronger than the case for analytical bias. Deciphering which parameter really played the major
24 512 role in our data set is made difficult by the fact that we are comparing data at the 0.1 permil level
25 513 which is very close to the limitations of the SIMS method. We also cannot exclude that the tiny
26 514 pyrite crystals that are well below the size of the SIMS beam (1 vs. 10 μm , respectively) in
27 515 impact breccia NWA 7533 show less negative $\Delta^{33}\text{S}$ compared to the larger crystals measured.
28 516 Clearly, resolving both issues will demand better spatial resolution and analytical precision than
29 517 those of present-day SIMS techniques .
30 518

31 518 **Hydrothermal cycling of MIF-bearing S in NWA 7533**

32 519 As recalled in the introduction, SNC meteorites that have sampled sub-effusive igneous
33 520 rocks of the martian crust (i.e. nakhlites) have provided multiple evidence of crustal S
34 521 contamination that took place throughout the cooling history of these rocks, from the magma
35 522 crystallization stage to late exposure to hydrothermal fluids and evaporitic brines (see also Dottin
36 523
37 524
38 525
39 526
40 527
41 528
42 529
43 530
44 531
45 532
46 533
47 534
48 535
49 536
50 537
51 538
52 539
53 540
54 541
55 542
56 543
57 544
58 545
59 546
60 547

1
2
3 523 et al., 2018; Franz et al., 2019; Bridges et al., 2019 and reference therein). These rocks produce
4
5 524 trends of positive $\delta^{34}\text{S}$ values coupled with negative $\Delta^{33}\text{S}$ values with water soluble (Ca sulfates)
6
7 525 and acid soluble sulfates (jarosite) in Antarctic nakhlites (McCubbin et al., 2009) defining the
8
9 526 highest $\delta^{34}\text{S}$ endmembers (Fig. 7). Likewise ALH 84001 (a proxy of NWA 7533 orthopyroxene
10
11 527 crystal clasts with similar ages of formation; Hewins et al., 2017) incorporated crustal sulfate
12
13 528 enriched in ^{34}S along with anomalous ^{33}S ($\delta^{34}\text{S} = 7.20 \pm 0.15\%$, $\Delta^{33}\text{S} = -0.072 \pm 0.008\%$, $\Delta^{36}\text{S} =$
14
15 529 $0.02 \pm 0.15\%$; Franz et al., 2014). We note here that the MIF observed in NWA 7533 (this
16
17 530 study) and in the nakhlites (Franz et al., 2014; Dottin et al., 2018) are an order of magnitude
18
19 531 smaller than the effects observed in terrestrial Archean pyrites (Farquhar et al., 2000). During the
20
21 532 photolysis of SO_2 , the magnitude of the S-MIF effect is dependent on the formation of at least
22
23 533 two distinct species, an oxidized sulfate (or gaseous SO_3) and a reduced sulfur polymer (S_2 or S_8)
24
25 534 between which the sulfur isotopes are distributed in a mass-independent manner (Pavlov and
26
27 535 Kasting, 2002). The presence of oxidation on Mars' surface evidenced by oxychlorine
28
29 536 compounds would oxidize the reduced species, so that practically all sulfur ends up as sulfate at
30
31 537 the surface. This would prevent the formation of large MIF effects in surficial sulfate, contrary to
32
33 538 initial expectations.

34
35 539 As suggested by NWA 7533 pyrite, negative $\delta^{34}\text{S}$ values seem to be a characteristic
36
37 540 feature of pyrite occurrences in SNC meteorites. Shearer et al. (1996) and Greenwood et al.
38
39 541 (2000) documented a wide range of $\delta^{34}\text{S}$ ($-9.69 \pm 0.22\%$ to $7.8 \pm 0.7\%$), as well as anomalous
40
41 542 $\Delta^{33}\text{S}$ signals ($-0.74 \pm 0.39\%$ and $-0.51 \pm 0.38\%$) in two pyrite grains located in "crushed zones"
42
43 543 of ALH 84001 and associated with carbonates interpreted to have hydrothermal origin. Negative
44
45 544 $\delta^{34}\text{S}$ values were also published for Lafayette pyrite resulting from partial replacement of
46
47 545 pyrrhotite by sulfur-bearing fluid influx into the nakhlite unit (Greenwood et al., 2000; Fig. 7).
48
49 546 The same is true for Chassigny pyrite that replaced pyrrhotite ($-4.6\% < \delta^{34}\text{S} < -1.5\%$; Greenwood
50
51 547 et al., 2000). According to Shearer et al. (1996) and Greenwood et al. (2000), igneous pyrrhotite
52
53 548 in ALH 84001 was largely converted to pyrite by a secondary alteration process, such as an
54
55 549 impact-driven hydrothermal system. A low-temperature (200°C) hydrothermal influx of volatile
56
57 550 components (S, C, H) was postulated for this reaction in Chassigny, too (Floran et al., 1978;
58
59 551 Peslier et al., 2019; Lorand et al., 2018a and references therein). Using results from the Sample
60
552 Analysis at Mars (SAM) facility aboard the Curiosity rover, Franz et al (2017) found large

1
2
3
4 553 variations in $\delta^{34}\text{S}$ in ten sites of fluvio-lacustrine sediments filling the Gale Crater that exceed
5
6 554 those measured for martian meteorites. They identified quite low $\delta^{34}\text{S}$ ($-47 \pm 14 \text{ ‰}$) at both
7
8 555 Cumberland (CB) and Oudam (OU) sites where sulfides (pyrrhotite, pyrite) occur and
9
10 556 enrichment in ^{34}S ($0 < \delta^{34}\text{S} < 28 \pm 7 \text{ ‰}$ (CDT normalized)) in mudstone-hosted sulfates. They
11
12 557 concluded that sulfur isotopic equilibrium between sulfides and sulfates could have
13
14 558 been reached through warmed groundwater within several thousand years at 100–
15
16 559 150°C to yield $\delta^{34}\text{S}$ depleted sulfides.

17
18 560 A similar process known as Thermochemical Sulfate Reduction (TSR) is assumed to
19
20 561 have transferred S-MIF-bearing S into martian impact breccias. Thermochemical Sulfate
21
22 562 Reduction is associated with kinetic fractionation that scales with temperature (Kiyosu and
23
24 563 Krouse, 1990). Anhydrite-pyrite fractionation coefficients indicate a difference of 15 per mil at
25
26 564 300°C (Shanks, 2014 and references therein) with more positive (heavier) compositions in
27
28 565 sulfates compared to pyrite. Typical TSR S isotope fractionations are usually less than 20 ‰
29
30 566 (Machel et al., 1995; Seal, 2006). A crude estimate for initial martian sulfate source enriched in
31
32 567 ^{34}S is suggested by $\delta^{34}\text{S}$ as high as $4.7 \pm 0.2\text{ ‰}$ in sulfate extracted from Nakhla (Farquhar et al.,
33
34 568 2007). Shergottite sulfates show $\delta^{34}\text{S}$ of $6.68 \pm 0.15\text{ ‰}$ (Farquhar et al., 2007). Higher values
35
36 569 recorded by sulfate of Antarctic nakhrites MIL 03346 and its pairs (up to 12.39 ‰) may reflect
37
38 570 input of terrestrial sulfates (Franz et al., 2014), but are not unrealistic for martian sulfates as
39
40 571 suggested by analyses of sulfate in fluvio-lacustrine sediments of Gale crater (Franz et al., 2017).
41
42 572 Hence, taking into account the extreme isotopic composition of martian sulfates, the isotopic
43
44 573 fractionation relationship between NWA 7533 pyrite and putative martian sulfates ($\delta^{34}\text{S}_{\text{sulfate}} -$
45
46 574 $\delta^{34}\text{S}_{\text{pyrite}}$) is about 10 ‰. Such $\delta^{34}\text{S}$ values require TSR temperatures in excess of 250°C using the
47
48 575 experimentally derived equation of Kiyosu and Krouse (1990) (see also Machel et al. (1995)). To
49
50 576 preserve negative $\delta^{34}\text{S}$ values, this system must have been open with respect to the supply of
51
52 577 sulfate (sulfate supply > sulfate consumption), otherwise pyrite would develop positive $\delta^{34}\text{S}$
53
54 578 values upon completion of closed system fractionation effects (e.g. Magnall et al., 2016). Such
55
56 579 an open system is consistent with the widespread distribution of pyrite inside porosity of each
57
58 580 lithological component of martian breccias, including late veinlets. The TSR process may have
59
60 581 contributed along with other petrogenetic processes (magma degassing, weathering.....) to the

1
2
3 582 highly oxidized state of NWA 7533 of \sim FMQ + 2 log units (Leroux et al., 2016; Hewins et al.,
4 583 2017), well above typical martian magmatic conditions. Reduction of one mole of S^{6+} to S^{2-}
5 584 consumes eight moles of electrons and has the potential to oxidize eight moles of Fe^{2+} to Fe^{3+}
6 585 (see detailed calculation in Dottin et al., 2018). Our scenario of precursor sulfates is also
7 586 supported by the S/Se ratio of NWA 7533 pyrite (3,500-54,000; Lorand et al. 2018b; Fig. 5).
8 587 Selenium chemistry is strongly tied to S chemistry: both elements can substitute as anions into
9 588 sulfides while forming oxycompounds hosted in sulfates (Howard, 1977; Huston et al., 1995;
10 589 Lorand et al., 2003; Ziemkiewicz et al., 2011 and references therein). Although Se concentration
11 590 data (and hence S/Se ratio) are not available for martian sulfates, one nakhlite (MIL 03346) that
12 591 bears multiple evidence of martian sulfate contamination shows a bulk-rock S/Se ratio of up to
13 592 13,385 whereas it is only 3566 ± 798 for the shergottites that have incorporated juvenile (mantle-
14 593 derived) martian sulfur (Wang and Becker, 2017). Owing to its S/Se ratio up to 54,000, there can
15 594 be little doubt that NWA 7533 pyrite formed from precursor sulfates (Fig. 6).

16 595 The Eh-pH redox conditions deduced for NWA 7533 from the Fe-S-O system, and the
17 596 lack of any firmly identified sulfate, imply that sulfate reduction products were recycled by
18 597 hydrothermal fluids in the martian breccia as reduced to near-neutral H_2S/HS^- -rich aqueous
19 598 fluids (Lorand et al., 2015). Reduction of sulfate during the hydrothermal process would
20 599 generate H_2S and potentially H_2Se that are likely to precipitate as pyrite in the presence of Fe^{2+}
21 600 (Auclair et al., 1987). Experimental studies on terrestrial hydrothermal vent systems demonstrate
22 601 that at 300 and 350 °C (a temperature range corresponding to that deduced from the Ni content
23 602 of NWA 7533 pyrite; Lorand et al., 2015, 2018b), pyrite is expected to be depleted in the heavy
24 603 isotopes of S relative to H_2S at equilibrium (Seal, 2006; Wu et al., 2010; Gregory et al., 2015;
25 604 Magnall et al., 2016). Lorand et al. (2015, 2018b) suggested that NWA 7533 pyrite precipitated
26 605 by direct nucleation or sulfidation reactions between H_2S/HS^- -rich aqueous fluids and Fe from
27 606 different sources (dissolved ions in the fluid, pyroxene clast, matrix oxides (magnetite,
28 607 maghemite)). Like pyrite, the negative $\Delta^{33}S$ coupled with negative $\delta^{34}S$ values makes the few
29 608 fine-grained spongy anhedral pyrrhotite grains identified in the interclast matrix (ICM) of NWA
30 609 7533 crystallization products from fluids that reduced crustal sulfates (Fig. 2). However, the
31 610 highly resorbed and denticulated shape of these pyrrhotite blebs and their spongy textures
32 611 compared to euhedral pyrite crystals are noteworthy. Such sulfide textures were reported in SNC
33 612 meteorites that experienced shock-induced sulfur degassing (Lorand et al., 2012, Gattaceca et al.,

1
2
3 613 2013). Lorand et al. (2012) concluded that pyrite in the strongly shocked chassignite NWA 2737
4 614 was desulfurized into FeS due the high shock pressure (55 GPa) coupled with strong heating
5 615 conditions (perhaps up to 800 °C) published for this meteorite. In NWA 7533, the shock event
6 616 postdating pyrite crystallization generated only planar deformation features in pyrite. A
7 617 desulfurization of pyrite into spongy pyrrhotite is thus considered to be very unlikely. For
8 618 comparison, pyrite was preserved in Chassigny that experienced a shock pressure of much
9 619 greater intensity (about 35 GPa with a post-shock temperature of about 300 °C; Lorand et al.,
10 620 2018a). The NWA 7533 spongy pyrrhotite must be interpreted as a metastable hydrothermal
11 621 product of sulfate reduction reactions reflecting local, transient more reducing conditions during
12 622 percolation by hydrothermal fluids (see Lorand et al., 2015).
13
14
15
16
17
18
19
20
21
22

624 **Meteorite impact vs. igneous intrusion as source of NWA 7533 hydrothermal pyrite?**

23
24 625 According to a detailed analysis of pyrite textures and its relationships with silicate
25 626 lithologies of NWA 7533, hydrothermal alteration took place at a very late stage of the history of
26 627 the meteorite during and after a lithification and annealing event that made the regolith breccia
27 628 very cohesive. This annealing event responsible for the lithification of the meteorite likely
28 629 occurred at ~1.4 Ga from the apatite U-Pb ages (Bellucci et al., 2015), the zircon lower intercept
29 630 ages and the K-Ar ages (Humayun et al., 2013; Lindsay et al., 2014; McCubbin et al., 2016;
30 631 Cassata et al., 2018) and the whole-rock $^{187}\text{Re}/^{187}\text{Os}$ model ages (Goderis et al., 2016). Taking
31 632 into account the Amazonian age of NWA 7533 pyrite, the water responsible for the hydrothermal
32 633 event on Mars was likely produced by melting of ice from a subsurface permafrost reservoir.
33 634 Chlorine was likely present too, as indicated by core-rim increase in Cl/F ratio of NWA 7533
34 635 apatite (Bellucci et al., 2016); however, Lorand et al. (2018b) suggested that the chlorine content
35 636 was significantly low when NWA 7533 pyrite precipitated because this sulfide shows very low
36 637 contents of the base metals (Cu, Zn...) that are preferentially transported by Cl-rich acidic fluids.
37 638 This hydrothermal cycling process bears similarities to that documented for nakhlites from the
38 639 Fe-carbonate + Ca-sulfates + halite veins: Changela and Bridges (2011) argued for an impact-
39 640 induced heating event which triggered upward percolation of H₂O-CO₂ fluids from buried ice
40 641 into the nakhlite igneous mass, although both upward and downward percolations were also
41 642 suggested (see Bridges et al., 2019 and reference therein). A downward percolation of sulfate-
42 643 bearing aqueous fluid is considered to be more likely for martian impact breccias; however the
43
44
45
46
47
48
49
50
51
52
53
54
55
56
57
58
59
60

1
2
3 644 source of heat that triggered this percolation, either an impact or a magmatic event is still
4 645 debated (Lindsay et al., submitted).

6 646 Meteorite impacts on rocky planetary bodies have the potential to initiate transient
7
8 647 hydrothermal systems if: (i) the target contains sufficient volatiles (e.g. liquid water or ice), and
9
10 648 (ii) a substantial heat source is generated (e.g. melt sheet, nearby pluton, raised geothermal
11
12 649 gradient) (Newsom, 1980; Abramov and Kring, 2004; Naumov, 2005; Osinski et al., 2013;
13
14 650 Koeberl, 2014). Sulfides are common hydrothermal products in impact craters on Earth and
15
16 651 mineralisation dominated by pyrite is thought to occur during the latest stages of cooling (Parnell
17
18 652 et al., 2010; Simpson et al., 2005; 2017). Geochemical modeling of impact-generated
19
20 653 hydrothermal systems for Mars also frequently return pyrite among hydrothermal products (e.g.
21
22 654 Schwenzer and Kring, 2013). As shown by these authors, pyrite becomes a major mineral along
23
24 655 with hematite for water/rock ratios exceeding 1,000. Such conditions are met inside veins, as
25
26 656 observed in NWA 7533 where some cracks are filled with pyrite + maghemite (Lorand et al.,
27
28 657 2015). Cassata et al. (2018) proposed for NWA 7034 (paired with NWA 7533) a rather different
29
30 658 interpretation linking the lithification and annealing event with a thermal dome above deeper
31
32 659 intrusives because thermal metamorphism recorded by the K-Ar and U-Pb systems yield plateau
33
34 660 age differences that were greater than durations (10's of Ma or less) required to cool shock-
35
36 661 heated basement terrains following large (100 to 200 km) impact events that might have
37
38 662 occurred at ~1,300 Ma. Magmatism is known to have occurred on Mars at 1.4-1.35 Ga from the
39
40 663 nakhlite and chassignite meteorites (Nyquist et al., 2001; Cohen et al., 2017 and references
41
42 664 therein), while the impact cratering rate of the martian surface was already considerably reduced
43
44 665 at that time (e.g., Moser et al., 2019). However, MacArthur et al. (2019) related the maximum
45
46 666 ^{40}Ar - ^{39}Ar age of 1130 – 1250 Ma in the NWA 8114 meteorite clast (paired with NWA 7533)
47
48 667 analysed by them to an impact shock event and the subsequent high-temperature oxidative
49
50 668 breakdown of many of the pyroxenes (also documented in NWA 7533 by Leroux et al., 2016). A
51
52 669 simple Fourier cooling model suggested that a burial depth of 5 m was enough to maintain
53
54 670 sufficiently high temperatures (>600°C) for ~30 days (MacArthur et al., 2019). With this
55
56 671 constraint in hand, one may assume that sulfates in martian breccias may have been reduced to
57
58 672 sulfides almost in-situ, implying very little transport of aqueous fluids.
59
60 673

674 CONCLUSIONS

1
2
3 675
4
5 676 Pyrite is by far the major host of sulfur in the polymict NWA 7533 breccia and paired
6
7 677 meteorites. Apatite and Fe oxyhydroxides are negligible S carriers, as are the tiny magmatic
8
9 678 sulfide grains so far identified. Sulfates (barite or gypsum) have not been firmly identified in the
10
11 679 breccia. The initial sulfur content of the breccia inferred from the modal abundance of pyrite and
12
13 680 its pseudomorphous Fe-oxyhydroxides is estimated to be ~5,400 ppm. The two bulk-rock S
14
15 681 analyses obtained here confirm previous estimates of 80% S loss resulting from terrestrial
16
17 682 weathering of NWA 7533 pyrite.

18 683
19 684 The occurrence of S-MIF in the S multi-isotope composition supports a model of NWA
20
21 685 7533 pyrite formation from martian surficial sulfur that experienced photochemical reaction(s).
22
23 686 The slight discrepancy between *in-situ* SIMS analyses ($\Delta^{33}\text{S} = -0.2 \pm 0.1 \text{ ‰}$; mean of 29
24
25 687 analyses) and the bulk IRMS analyses ($\Delta^{33}\text{S} = -0.029 \pm 0.010 \text{ ‰}$) is tentatively interpreted as a
26
27 688 likely sampling bias since only grains > 20 μm in size were analyzed.

28
29 689 Negative $\delta^{34}\text{S}$ values were previously reported for several occurrences of secondary
30
31 690 pyrite in SNC meteorites. Such negative values in the hydrothermal setting of NWA 7533 are
32
33 691 reflective of authigenic sulfide precipitated from H_2S produced via open-system reduction of
34
35 692 sulfates. A transient more reducing stage likely produced the spongy pyrrhotite that carries
36
37 693 similar S multi-isotope compositions as that of pyrite.

38
39 694 It is concluded that sulfur was recycled by downward percolation of reduced S-bearing
40
41 695 aqueous fluid produced by melting of permafrost. However, the driving force that recycled
42
43 696 crustal S in NWA 7533 lithologies, underlying magmatic intrusions or impact-induced heating,
44
45 697 is presently unclear.

46
47 698
48 699 **Acknowledgement** We are indebted to L. Labenne for the sample. We are grateful for funding
49
50 700 from CNES-INSU grant 2014-PNP (J.-P. L.) and the Agence Nationale de la Recherche (ANR)
51
52 701 under the contract ANR16CE310012 entitled Mars Prime. The LA-ICP-MS facility at the LPG
53
54 702 Nantes was established by funds from the Region Pays de la Loire. Carole La is thanked for her
55
56 703 help with the LA-ICP-MS facility at LPG Nantes; MH was supported by NASA Solar System
57
58 704 Workings (NNX16AP98G). The National High Magnetic Field Laboratory is supported by the
59
60 705 National Science Foundation through NSF/DMR-1644779 and the state of Florida. The revised
61
62 706 version was greatly improved thanks to comments from three reviewers and associate

1
2
3 707 editor Cyrena Goodrich.
4
5

6 708

7 709

8 710

9 711

10 712

REFERENCES

11
12
13 713 Abramov O. and Kring D. A. 2005. Impact-induced hydrothermal activity on early Mars.

14 714 *Journal of Geophysical Research* 110:E12S09. doi:10.1029/ 2005JE002453.

15
16 715 Agee C. B., Wilson N. V., McCubbin F. M., Ziegler K., Polyak V.J., Sharp Z. D., Asmerom Y.,

17 716 Nunn M. H., Shaheen R., Thiemens M. H., Steele A., Fogel M. L., Bowden R., Glamoclija

18 717 M., Zhang Z. and Elardo S. M. 2013. Unique meteorite from Early Amazonian Mars:

19 718 water-rich basaltic breccia Northwest Africa 7034. *Science* 339:780–785.

20 719 Auclair G., Fouquet Y., and Bohn M. 1987. Distribution of selenium in high-temperature

21 720 hydrothermal sulfide deposits at 13° North, East Pacific Rise. *Canadian Mineralogist* 25:

22 721 577-588.

23 722 Baumgartner R., Fiorentini M., Lorand J.-P., Baratoux D., Zaccarini F., Ferrière L., Prasek M.

24 723 and Sener K. 2017. The role of sulfides in the fractionation of highly siderophile and

25 724 chalcophile elements during the formation of martian shergottite meteorites. *Geochimica et*

26 725 *Cosmochimica Acta* 210: 1-24.

27 726 Bellucci J. J., Nemchin A. A., Whitehouse M. J., Humayun M., Hewins R. and Zanda B. 2015.

28 727 Pb-isotopic evidence for an early, enriched crust on Mars. *Earth & Planetary Science*

29 728 *Letters* 410:34-41.

30 729 Bellucci J. J., Whitehouse M. J., Nemchin A.A., Snape J.F., Kenny, G.G., Merle R.E., Bland

31 730 P.A. & Benedix G.K. 2020. Tracing martian surface interactions with the triple O isotope

32 731 compositions of meteoritic phosphates." *Earth & Planetary Science Letters* 531:115977.

33 732 Bridges J. C. and Grady M. M. 2000. Evaporite mineral assemblages in the nakhlite (martian)

34 733 meteorites. *Earth & Planetary Science letters* 176:267-279.

35 734 Bridges J., Hicks J.M. and Treiman A.H. 2019. Carbonates on Mars. "Volatiles in the Martian

36 735 crust" edited by Filiberto J. and Schwenzer S. P. Amsterdam: Elsevier. pp. 89–118.

- 1
2
3 736 Cassata W. S., Cohen B. E., Mark D. F., Trappitsch R., Crow C. A., Wimpenny J., Lee M. R.
4 and Smith C. L. 2018. Chronology of martian breccia NWA 7034 and the formation of the
5 737 martian crustal dichotomy. *Sci. Adv.* 4, eaap 8306, 11 pp.
6 738
7
8 739 Changela H. G. and Bridges J. C. 2011. Alteration assemblages in the nakhlites: Variation with
9 740 depth on Mars. *Meteoritics & Planetary Sciences* 45:1847-1867.
10
11 741 Chevrier V., Lorand J.-P. and Sautter V. 2011. Sulfide petrology of four nakhlites (NWA817,
12 742 NWA998, Nakhla, Governador Valadares). *Meteoritics & Planetary Sciences* 46: 769-784.
13
14 743 Dehouck E., Chevrier V., Gaudin A., Mangold N., Mathe P.E. and Rochette P. 2012. Evaluating
15 744 the role of sulfide-weathering in the formation of sulfates or carbonates on Mars.
16 745 *Geochimica et Cosmochimica Acta* 90:47-63.
17
18 746 Dottin J.W., Labidi J., Farquhar J., Piccoli P., Liu M.-C. and McKeegan K.D. 2018. Evidence for
19 747 oxidation at the base of the nakhlite pile by reduction of sulfate salts at the time of lava
20 748 emplacement. *Geochimica et Cosmochimica Acta* 239:186–197.
21
22 749 Farquhar J., Kim S.-T. and Masterson, A. 2007. Implications from sulfur isotopes of the Nakhla
23 750 meteorite for the origin of sulfate on Mars. *Earth Planetary Science Letters* 264:1-8.
24
25 751 Farquhar J., Savarino J., Airieau S. and Thiemens M. H. 2001. Observation of wavelength-
26 752 sensitive mass-independent sulfur isotope effects during SO₂ photolysis: Implications for
27 753 the early atmosphere. *Journal of Geophysical Research* 106:32829-32839.
28
29 754 Farquhar J., Savarino J., Jackson T. L. and Thiemens M. H. 2000. Evidence of atmospheric
30 755 sulfur in the martian regolith from sulfur isotopes in meteorites. *Nature* 404:50-52.
31
32 756 Floran R.J., Prinz M., Hlava P.F., Keil K., Nehru C.E. and Hinthorne J.R., 1978. The Chassigny
33 757 meteorite: A cumulate dunite with hydrous amphibole-bearing melt inclusions. *Chemical*
34 758 *Geology* 42, 1213-1222.
35
36 759 Foley C.N., Economou T., and Clayton R.N. 2003. Final chemical results from the Mars
37 760 Pathfinder Alpha Proton X-ray Spectrometer. *Journal of Geophysical Research* **108**, 8096,
38 761 DOI: 10.1029/2002JE002019.
39
40 762 Franz H.H, Kim S.T., Farquhar J., Day J.M.D., Economos R.C., McKeegan K., Schmitt A.K.,
41 763 Irving A.J., Hoek J. and Dottin J. III 2014. Isotopic links between atmospheric chemistry
42 764 and the deep sulfur cycle on Mars. *Nature* 508:365-368.
43
44 765 Franz H. B., McAdam A., Ming D. W., Freissinet C., Mahaffy P. R., Eldridge D. L.,
45 766 Fischer W. F., Grotzinger J. P., House C. H., Hurowitz J. A., McLennan S. M.,

- 1
2
3 767 Schwenzer S. P., Vaniman D. T., Archer P. D. Jr, Atreya S. K., Conrad P. G., Dottin J.
4
5 768 W. III, Eigenbrode J. L., Farley K. A., Glavin D. P., Johnson S. S., Knudson C. A.,
6
7 769 Morris R.V., Navarro-Gonzalez R., Pavlov A.A., Plummer R., Rampe E. B., Stern J.
8
9 770 C., Steele A., Summons R. E., and Sutter B. 2017. Large sulfur isotope fractionations
10
11 771 in Martian sediments at Gale crater. *Nature Geoscience* 10:658–662.
- 12
13 772 Franz H. B., King P. L. and Gaillard F. 2019. Sulfur on Mars from the atmosphere to the
14
15 773 core. In “Volatiles in the Martian crust” edited by Filiberto J. and Schwenzer S. P.
16
17 774 Amsterdam: Elsevier. pp. 119–183.
- 18
19 775 Gaillard F., Michalski J., Berger G., McLennan S.M. and Scaillet B. 2013. Geochemical
20
21 776 reservoirs and timing of sulfur cycling on Mars. *Space Science Review* 174, 251-300
- 22
23 777 Gattacceca, J., Hewins, R.J., Lorand, J.-P., Rochette, P., Lagroix, F., Cournède, C., Uehara, M.,
24
25 778 Pont, S., Sautter, V., Scorzelli, R.B., Hombourger, C., Munayco, P., Zanda, B., Chennaoui,
26
27 779 H., 2013. Opaque minerals, magnetic properties and paleomagnetism of the Tissint
28
29 780 Martian meteorite. *Meteoritics & Planetary Sciences* 48, 10, 1919-1936.
- 30
31 781 Gattacceca J., Rochette P., Scorzelli R.B., Munayco P., Agee C., Quesnel Y., Cournède C. and J.
32
33 782 Geissman J. 2014. Martian meteorites and Martian magnetic anomalies: A new perspective
34
35 783 from NWA 7034, *Geophysical Research Letters* 41, 4859–4864,
36
37 784 doi:10.1002/2014GL060464.
- 38
39 785 Goderis S., Brandon A. D., Mayer B. and Humayun M. 2016. Ancient impactor components
40
41 786 preserved and reworked in martian regolith breccia Northwest Africa 7034. *Geochimica et*
42
43 787 *Cosmochimica Acta* 191, 203–215.
- 44
45 788 Gooding J.L., Wentworth S.J. and Zolensky M. 1991. Aqueous alteration of the Nakhla
46
47 789 meteorite. *Meteoritics* 326: 135-143.
- 48
49 790 Greenwood J. P., Mojzsis S. J. and Coath C. D 2000. Sulfur isotopic compositions of individual
50
51 791 sulfides in martian meteorites ALH 84001 and Nakhla: Implications for crust-regolith
52
53 792 exchange on Mars. *Earth & Planetary Science Letters* 184:23-35.
- 54
55 793 Greenwood J. P., Riciputi L. R., McSween H. Y. Jr. and Taylor L. A. 2000. Modified sulfur
56
57 794 isotopic compositions of sulfides in the nakhlites and Chassigny. *Geochimica et*
58
59 795 *Cosmochimica Acta* 64, 1121-1131.
- 60

- 1
2
3 796 Gregory D.D., Large R. R., Halpin J.A., Steadman J.A., Hickman H.E., Ireland, T.E. and Holden
4
5 797 P. 2015. A degree of sulfate reduction in an open system to produce negative $\delta^{34}\text{S}$.
6
7 798 *Geochimica et Cosmochimica Acta* 150:223–250.
- 8
9 799 Griffin W.L., Powell W.J., Pearson N.J. and O'Reilly S.Y. 2008. GLITTER: Data reduction
10
11 800 software for laser ablation ICP-MS: *Mineral Association of Canada Short Course Series*
12
13 801 40, pp. 308–311.
- 14 802 Gröger, J., Franke, J., Hamer, K. and Schulz, H.D., 2009. Quantitative recovery of elemental
15
16 803 sulfur and improved selectivity in a chromium-reducible sulfur distillation. *Geostandards*
17
18 804 *and Geoanalytical Research* 33(1), pp.17-27.
- 19 805 Grotzinger J.P., Sumner D. Y., Kah L., Stack C. K., Gupta S., Edgar L., Rubin D., Lewis
20
21 806 K., Schieber J., Mangold N., Milliken R., Conrad P.G., DesMarais D., Farmer J.,
22
23 807 Siebach K., Calef K., Hurowitz J., McLennan S. M., Ming D., Vaniman D., Crisp J.,
24
25 808 Vasavada A., Edgett K.S., Malin M., Blake D., Gellert R., Mahaffy P., Wiens R. C.,
26
27 809 Maurice S., Grant J. A., Wilson S., Anderson R. C., Beegle L., Arvidson R., Hallet
28
29 810 B., Sletten R. S., Rice M., Bell III J., Griffes J., Ehlmann B., Anderson R. B., Bristow
30
31 811 T. F. , Dietrich W. E., Dromart G., Eigenbrode J., Fraeman A., Hardgrove C.,
32
33 812 Herkenhoff K., Jandura L., Kocurek G., Lee S., Leshin L. A., Leveille R., Limonadi
34
35 813 D., Maki J., McCloskey S., Meyer M., Minitti M., Newsom H., Oehler D., Okon A.,
36
37 814 Palucis M., Parker T., Rowland S., Schmidt M., Squyres S., Steele A., Stolper E.,
38
39 815 Summons R., Treiman A., Williams R., Ayingst ., MSL Science Team 2014. A
40
41 816 Habitable Fluvio-Lacustrine Environment at Yellowknife Bay, Gale Crater, Mars.
42
43 817 *Science*, 343 1242777-1-14.
- 44
45
46 818 Hewins R. H., Zanda B., Humayun M., Nemchin A., Lorand J.-P., Pont S., Deldicque D.,
47
48 819 Bellucci J. J., Beck P., Leroux H., Marinova M., Remusat L., Göpel C., Lewin E., Grange
49
50 820 M., Kennedy A. and Whitehouse M. (2017) Regolith breccia Northwest Africa 7533:
51
52 821 mineralogy and petrology with impli- cations for early Mars. *Meteoritics & Planetary*
53
54 822 *Sciences* 52: 89–124.

- 1
2
3 823 Howard J. H. 1977. Geochemistry of Se: formation of ferroselite and Se behavior in the vicinity
4 of oxidizing sulfide and uranium deposits. *Geochimica et Cosmochimica Acta* 41:1665–
5 824 1678.
6
7 825
8 826 Humayun M., Nemchin A., Zanda B., Hewins R.H., Grange M., Kennedy M., Lorand J.-P.,
9 Göpel C., Pont S., Fieni C. and Deldicque D. 2013. Origin and age of the earliest martian
10 827 crust from meteorite NWA 7533. *Nature* 503:513-516.
11 828
12
13 829 Humayun M., Hewins R. H., Lorand J.-P., and Zanda B. 2014. Weathering and impact
14 melting determined the mineralogy of the early Martian crust preserved in
15 830 Northwest Africa 7533 (abstract #1880). *45th Lunar and Planetary Science Conference*.
16 831 CD-ROM.
17 832
18
19 833 Huston D. L., Sie S. H., Suter G. F., Cooke D. R. and Both R. A. 1995. Trace elements in sulfide
20 834 minerals from eastern Australian volcanic-hosted massive sulfide deposits; Part I, Proton-
21 835 microprobe analyses of pyrite, chalcopyrite, and sphalerite, and Part II, selenium levels in
22 836 pyrite; comparison with $\delta^{34}\text{S}$ values and implications for the source of sulfur in
23 837 volcanogenic hydrothermal systems. *Economic Geology* 90:1167–1196.
24
25 838 Kerber L., Forget F. and Wordsworth R. 2015. Sulfur in the early Martian atmosphere revisited:
26 839 Experiments with a 3-D Global Climate Model. *Icarus* 261:133–148.
27
28 840 King P.L. and McLennan S.M. 2010. Sulfur on Mars. *Elements* 6:107-112.
29
30 841 Kiyosu Y. and Krouse R. H. 1990. The role of organic and acid in the in the sulfur abiogenic
31 842 isotope reduction effect. *Geochemistry Journal* 24:21-27.
32
33 843 Koeberl C. 2014. The geochemistry and cosmochemistry of impacts. In: Planets, Asteroids,
34 844 Comets and The Solar System. In: *Treatise on Geochemistry, vol.2, 2nd edition*. Elsevier,
35 845 pp.73–118.
36
37 846 Labidi J., Cartigny P., Birck J. L., Assayag N. and Bourrand J. J. 2012. Determination of
38 847 multiple sulfur isotopes in glasses: a reappraisal of the MORB $\delta^{34}\text{S}$. *Chemical Geology* 334:
39 848 189–198.
40
41 849 Labidi J., Farquhar J., Alexander C.M.O.D., Eldridge D.L., Oduro H. 2017. Mass independent
42 850 sulfur isotope signatures in CMs: Implications for sulfur chemistry in the early solar system,
43 851 *Geochimica et Cosmochimica Acta* 196:326-350.

- 1
2
3 852 Leroux H., Jacob D., Marinova M., Hewins R. H., Zanda B., Pont S., Lorand J.-P. and Humayun
4
5 853 M. 2016. Exsolution and shock microstructures of igneous pyroxene clasts in the NWA
6
7 854 7533 Martian meteorite. *Meteoritics & Planetary Sciences* 51:932–945.
- 8
9 855 Lindsay F. N., Turri, B. D., Göpel C., Herzog G. F., Zanda B., Hewins R., Park J., Delaney J. S.
10
11 856 and Swisher C. C. 2014. $^{40}\text{Ar}/^{39}\text{Ar}$ Ages of Martian Meteorite NWA 7533. *Meteoritics &*
12
13 857 *Planetary Sciences* 47, Abstract #5383.
- 14 858 Lindsay F. N., Delaney J. S., Göpel C., Herzog G. F., Hewins R. H., Humayun M., Nagao K.,
15
16 859 Nyquist L. E., Park J., Setera J. B., Shih C.-Y., Swisher C. C., III, Zanda B. and Turrin B. D.
17
18 860 (2020) $^{40}\text{Ar}/^{39}\text{Ar}$ ages of Northwest Africa 7034 and Northwest Africa 7533. *Meteoritics &*
19
20 861 *Planetary Sciences* (submitted; MaPS 3348).
- 21 862 Lorand J.-P., Alard O., Luguet A. and Keays R. R. 2003. S/Se systematics of the subcontinental
22
23 863 lithospheric mantle beneath the Massif Central. *Geochimica et Cosmochimica Acta*
24
25 864 67:4137–4153.
- 26 865 Lorand, J.-P., Barat, J.-A., Chevrier, V., Sautter, V. and Pont, S., 2012. Metal-saturated sulfide
27
28 866 assemblages in chassignite NWA 2737; evidence for impact-related sulfur devolatilisation.
29
30 867 *Meteoritics & Planetary Sciences* 47:1830-1841.
- 31 868 Lorand J.-P., Hewins R. H., Pont S., Zanda B., Humayun M. Nemchin A. and others 2015.
32
33 869 Nickeliferous pyrite tracks pervasive hydrothermal alteration in martian regolith breccia : a
34
35 870 study in NWA 7533. *Meteoritics & Planetary Sciences* 50:2099-2120.
- 36 871 Lorand J.-P., Pont S., Chevrier V., Luguet A., Zanda B. and Hewins R. H. 2018(a). Petrogenesis
37
38 872 of martian sulfides in the Chassigny meteorite. *American Mineralogist*, special issue
39
40 873 “Planetary Sulfides” 103:872-885.
- 41 874 Lorand J.-P., Hewins R. H., Humayun M., Zanda B., Remusat L., La C. and Pont S. 2018(b).
42
43 875 Chalcophile-siderophile element systematics of hydrothermal pyrite from martian regolith
44
45 876 breccia NWA 7533. *Geochimica et Cosmochimica Acta* 241:134-149.
- 46 877 MacArthur J. C. Bridges L. J. Hicks Burgess R. Joy, K. H. Branney, M. J. Hansford G. M.,
47
48 878 Baker S. H., Schwenzer S. P., Gurman S. J., Stephen N. R., Steer E. D., Pierc J. D. and
49
50 879 Ireland T. R. 2019. Mineralogical constraints on the thermal history of martian regolith
51
52 880 breccia Northwest Africa 8114. *Geochimica et Cosmochimica Acta* 246:267-298.
- 53 881 Machel H. G., Krouse H. R. and Sassen R. 1995. Products and distinguishing criteria of bacterial
54
55 882 and thermochemical sulfate reduction. *Applied Geochemistry* 10:373–389.
- 56
57
58
59
60

- 1
2
3 883 Magnall J.M., Gleeson S.A., Stern R.A., Newton R.J., Poulton S.W. and Paradis S. 2016. Open
4
5 884 system sulfate reduction in a diagenetic environment – Isotopic analysis of barite ($\delta^{34}\text{S}$ and
6
7 885 $\delta^{18}\text{O}$) and pyrite ($\delta^{34}\text{S}$) from the Tom and Jason Late Devonian Zn–Pb–Ba deposits, Selwyn
8
9 886 Basin, Canada. *Geochimica et Cosmochimica Acta* 180:146–163.
- 10
11 887 Mari N., Riches A.J.V., Hallis L.J., Marrocchi Y., Villeneuve J., Gleissner P., Becker H. and Lee,
12
13 888 M., 2019. Syneruptive incorporation of martian surface sulphur in the nakhlite lava flows
14
15 889 revealed by S and Os isotopes and highly siderophile elements : implication for mantle
16
17 890 sources in Mars. *Geochimica et Cosmochimica Acta* 266:416-43.
- 18
19 891 Masterson A.L., Farquhar J. and Wing B. A. 2011. Sulfur mass-independent fractionation
20
21 892 patterns in the broadband UV photolysis of sulfur dioxide: Pressure and third body effects .
22
23 893 *Earth & Planetary Science letters* 306:253-260.
- 24
25 894 McCubbin F. M., Tosca N. J., Smirnov A., Nekvasil H., Steele A., Fries M. and Lindsley D. H.
26
27 895 2009. Hydrothermal jarosite and hematite in a pyroxene-hosted melt inclusion in martian
28
29 896 meteorite Miller Range (MIL) 03346: Implications for magmatic-hydrothermal fluids on
30
31 897 Mars. *Geochimica et Cosmochimica Acta* 73:4907-4917.
- 32
33 898 McCubbin F. M., Boyce J. W., Nova 'k-Szabo' T., Santos A. R., Tartese R., Muttik N., Domokos
34
35 899 G., Vazquez J., Keller L. P., Moser D. E., Jerolmack D. J., Shearer C. K., Steele A., Elardo
36
37 900 S. M., Rahman Z., Anand, M., Delhaye T. and Agee C. B. 2016. Geologic history of
38
39 901 Martian regolith breccia Northwest Africa 7034: evidence for hydrothermal activity and
40
41 902 lithologic diversity in the Martian crust. *Journal of Geophysical Research* 121: 2120-2149.
- 42
43 903 McLennan S.M., Bell J.F., Calvin M., Christensen P.R., Clark B.C., De Souza P.A., Farmer J.,
44
45 904 Farrand W.H., Fike D.A., Gellert R., Ghosh A., Glotch T.D., Grotzinger J.P., Hahn B.,
46
47 905 Herkenhoff K.E., Huorwitz J.A., Johnson J.R., Yen A., 2005. Provenance and diagenesis of
48
49 906 the evaporite-bearing Burns formation, Meridiani Planum, Mars. *Earth & Planetary
50
51 907 Science Letters* 240, 95–121.
- 52
53 908 Moser D. E., Arcuri G. A., Reinhard D. A., White L. F., Darling J. R., Barker I. R., Larson D. J.,
54
55 909 Irving A. J., McCubbin F. M., Tait K. T., Roszjar J., Wittmann A. and Davis C. 2019.
56
57 910 Decline of giant impacts on Mars by 4.48 billion years ago and an opportunity for early
58
59 911 habitability. *Nature Geoscience* 12:522-527.
- 60
912 Muller E., Philippot P., Rollion-Bard C. and Cartigny P. 2016. Multiple sulfur-isotope signatures
in Archean sulfates and their implications for the chemistry and dynamics of the early

- 1
2
3 914 atmosphere. *Proceedings of the National Academy of Sciences* 113:7432-7437.
- 4
5 915 Muller, E., Philippot, P., Rollion-Bard, C., Cartigny, P., Assayag, N., Marin-Carbonne, J., and
6
7 916 Sarma, D. S. 2017. Primary sulfur isotope signatures preserved in high-grade Archean
8
9 917 barite deposits of the Sargur Group, Dharwar Craton, India. *Precambrian Research*
10
11 918 295:38-47.
- 12 919 Nachon M., Clegg S. M., Mangold N., Schroder S., Kah L. C., Dromart G., Ollila A.,
13
14 920 Johnson J. R., Oehler D. Z., Bridges J. C., Le Mouelic S., Forni O., Wiens R. C.,
15
16 921 Anderson R. B., Blaney D. L., Bell J. F. I., Clark B., Cousin A., Dyar M. D., Ehlmann
17
18 922 B., Fabre C., Gasnault O., Grotzinger J., Lasue J., Lewin E., Leveille R., McLennan
19
20 923 S., Maurice S., Meslin P. Y., Rapin W., Rice M., Squyres S. W., Stack K., Sumner D.
21
22 924 Y., Vaniman D., and Wellington D. 2014. Calcium sulfate veins characterized by
23
24 925 ChemCam/Curiosity at Gale crater, Mars. *Journal of Geophysical Research Planets*
25
26 926 119:1991–2016.
- 27
28 927 Naumov M. 2005. Principal features of impact-generated hydrothermal circulation systems:
29
30 928 mineralogical and geochemical evidence. *Geofluids* 5:165–180.
- 31
32 929 Newsom H. E. 1980. Hydrothermal alteration of impact melt sheets with implications for Mars.
33
34 930 *Icarus* 44:207–216.
- 35 931 Nyquist L.E., Bogard D.D., Shii C.Y., Greshake A., Stöffler D., and Eugster O. 2001. Ages and
36
37 932 geological histories of Martian meteorites. *Space Science Reviews* 96:105–164.
- 38
39 933 Ohno S., Wing B., Rumble D. and Farquhar J. 2006. High precision analysis of all four stable
40
41 934 isotopes of sulfur (^{32}S , ^{33}S , ^{34}S and ^{36}S) at nanomole levels using a laser fluorination
42
43 935 isotope-ratio-monitoring gas chromatography-mass spectrometry. *Chemical Geology*
44
45 936 225:30-39.
- 46
47 937 Osinski G.R., Tornabene L.T., Banerjee N.R., Cockell C.S., Flemming R., Izawa M.R.,
48
49 938 McCutcheon J., Parnell J., Preston L.J., Pickersgill A.E., Pontefract A., Sapers H. and
50
51 939 Southam G., 2013. Impact-generated hydrothermal systems on Earth and Mars. *Icarus* 347–
52
53 940 363.
- 54 941 Parat F., Holtz F. and Streck M. 2011. Sulfur-bearing magmatic accessory minerals. *Review*
55
56 942 *Mineralogy and Geochemistry* 73:285-314.

- 1
2
3 943 Parnell J., Taylor W.C., Thackrey S., Osinski G.R. and Lee P. 2010. Permeability data for impact
4 breccias imply focused hydrothermal fluid flow. *Journal of Geochemical Exploration* 106:
5 944 171–175.
6
7 945
8 946 Pavlov A.A. and Kasting J.F. 2002. Mass-independent fractionation of sulfur isotopes in
9 Archean sediments: Strong evidence for an anoxic Archean atmosphere. *Astrobiology* 2:27–
10 947 41.
11
12 948
13 949 Peslier A. H., Hervig R., Yang S., Humayun M., Barnes J.J., Irving A. J. and Brandon A. D.
14 2019. Determination of the water content and D/H ratio of the martian mantle by
15 950 unravelling degassing and crystallization effects in nakhlites. *Geochimica et Cosmochimica*
16 951 *Acta* 266: 382-415.
17
18 952
19 953 Philippot P., Van Zuilen M. and Rollion-Bard C 2012. Variations in atmospheric sulfur
20 954 chemistry on early Earth linked to volcanic activity. *Nature Geoscience* 5:668–674.
21
22 955 Pierazzo E. and Artemieva, N. 2012. Local and Global Environmental Effects of Impacts on
23 956 Earth. *Elements* 8:55-60.
24
25 957 Righter K., Pando K. and Danielson L. R. 2009. Experimental evidence for sulfur-rich martian
26 958 magmas: Implications for volcanism and surficial sulfur sources. *Earth & Planetary Science*
27 959 *Letters* 288: 235-243.
28
29 960 Righter K., Abell P., Agresti D., Berger E.L., Burton A.S., Delaney J. S., Fries M.D.,
30 961 Gibson E.K., Haba M.K., Harrington A., Herzog G.F., Keller L.P., Locke D., Lindsay
31 962 F.N., McCoy T.J., Morris R.V., Nagao K., Nakamura-Messenger K., Niles P.B.,
32 963 Nyquist L.E., Park J., Peng Z.X.F., Shii C.Y., Simon J.I., Swisher C.C., Tappa M.J.,
33 964 Turrin B.D. and Zeigler R.A 2015. Mineralogy, petrology, chronology, and exposure
34 965 history of the Chelyabinsk meteorite and parent body. *Meteoritics & Planetary*
35 966 *Science* 50:1790–1819.
36
37 967 Schwenger S.P. and Kring, D.A. 2013. Alteration minerals in impact-generated hydrous
38 968 alteration systems- Exploring host rock variability. *Icarus* 226: 487-496.
39
40 969 Seal R. 2006. Sulfur isotope geochemistry of sulfide minerals. *Review in Mineralogy and*
41 970 *Geochemistry* 61:633–677.
42
43
44
45
46
47
48
49
50
51
52
53
54
55
56
57
58
59
60

- 1
2
3 971 Shanks W.C., III. 2014. Stable Isotope Geochemistry of Mineral Deposits. *Treatise of*
4 *Geochemistry* 2nd edition, Chap. 13.3, pp. 59-85 Elsevier (Carlson and Turekian, eds.)
5 972 <http://dx.doi.org/10.1016/B978-0-08-095975-7.01103-7>.
6 973
7
8 974 Shearer C. K., Layne G. D., Papike J. J. and Spilde M. N. 1996. Sulfur isotopic systematics in
9 alteration assemblages in martian meteorite Allan Hills 84001. *Geochimica et*
10 *Cosmochimica Acta* 60:2921-2926.
11 975
12 976
13 977 Simpson S.L., Boyce A.J., Lambert P., Lindgren P. and Lee M.R. 2017. Evidence for an impact-
14 induced biosphere from the $\delta^{34}\text{S}$ signature of sulfides in the Rochechouart impact structure,
15 France. *Earth & Planetary Science Letters* 460:192–200.
16 978
17 979
18 980 Simpson S.L., Osinski G.R., Lee P., Parnell J., Spray J.G. and Baron M. 2005. A case study of
19 impact-induced hydrothermal activity: the Haughton impact structure, Devon Island,
20 Canadian High Arctic. *Meteoritics & Planetary Sciences* 40:1859–1877.
21 981
22 982
23 983 Squyres S.W., Arvidson R.E., Bell J.F., Calef F., Clark B.C., Cohen B.A., Crumpler L.A., de
24 Souza P.A., Farrand W.H., Gellert R., Grant J., Herkenhoff K.E., Hurowitz J.A., Johnson
25 J.R., Jolliff B.L., Knoll A.H., Li R., McLennan S.M., Ming D.W., Mittlefehldt
26 D.W., Parker T.J., Paulsen G., Rice M.S., Ruff S.W., Schröder C., Yen A.S., Zacny K.
27 985
28 986
29 987 2012. Ancient impact and aqueous processes at Endeavour Crater, Mars. *Science* 336:570-
30 576.
31 988
32
33 989 Syverson D.D., Ono S., Shanks W.C. and Seyfried W.C. Jr. 2015. Multiple sulfur isotope
34 fractionation and mass transfer processes during pyrite precipitation and recrystallization:
35 An experimental study at 300 and 350°C. *Geochimica et Cosmochimica Acta* 165:418–434.
36 990
37 991
38 992 Thomassot E., Cartigny P., Harris J., Lorand J.-P., Rollion-Bard C. and Chaussidon M. 2009
39 Metasomatic diamond growth: A multi-isotope study (^{13}C , ^{15}N , ^{33}S , ^{34}S) of sulfide
40 inclusions and their host diamonds from Jwaneng (Botswana). *Earth & Planetary Science*
41 *Letters* 282: 79-90.
42 993
43 994
44 995
45 996 Tian F., Mark W., Claire B., Jacob D., Haqq M., Smith M., Crisp D.C., Catling D., Zahnle K.,
46 and Kasting J.F., 2010. Photochemical and climate consequences of sulfur outgassing on
47 early Mars. *Earth & Planetary Science Letters* 295:412–418.
48 997
49 998
50 999 Wentworth S.J. and Gooding J.L. 1994. Carbonates and sulfates in the Chassigny meteorite:
51 Further evidence for aqueous chemistry on the SNC parent planet. *Meteoritics &*
52 *Planetary Sciences* 29:860–863.
53 1000
54 1001
55
56
57
58
59
60

- 1
2
3 1002 Whitehouse M.J. 2013. Multiple Sulfur Isotope Determination by SIMS: Evaluation of
4
5 1003 Reference Sulfides for $\Delta^{33}\text{S}$ with Observations and a Case Study on the Determination of
6
7 1004 $\Delta^{36}\text{S}$. *Geostandard & Geoanalytical Research* 37:19–33.
- 8 1005 Wu N., Farquhar J., Strauss H., Kim S. and Canfield D. 2010. Evaluating the S-isotope
9
10 1006 fractionation associated with Phanerozoic pyrite burial. *Geochimica et Cosmochimica Acta*
11
12 1007 74:2050-2071.
- 13 1008 Ziemkiewicz P.F., O’Neal M. and Lovett R.J. 2011. Selenium leaching kinetics and in situ
14
15 1009 control. *Mineral Water Environment*. 30:141–150.

16 1010
17 1011
18 1012
19
20
21
22
23
24
25
26
27
28
29
30
31
32
33
34
35
36
37
38
39
40
41
42
43
44
45
46
47
48
49
50
51
52
53
54
55
56
57
58
59
60

1
2
3 **1013 Figure caption**

4 1014
5 1015 Figure 1 : Backscattered electron (BSE) images of NWA 7533 Fe sulfides. (A) euhedral
6 1016 pyrite (1) affected by late fracturing that also guided terrestrial weathering (2) dark gray
7 1017 Fe oxyhydroxides); (B) poikilitic pyrite surrounded by a fine-grained dust of ICM
8 1018 minerals; solid inclusions are skeletal Fe oxides (maghemite-magnetite; 3) and perfectly
9 1019 euhedral apatite (4); (C) interstitial porous pyrrhotite (5) within interclast matrix (ICM).
10 1020 Note silicate clast inclusions (I) in the pyrrhotite.

11
12
13
14
15
16
17
18 1021 Figure 2 : $\delta^{34}\text{S}$ vs $\Delta^{33}\text{S}$ diagram for NWA 7533 sulfides and bulk-rock. $\Delta^{33}\text{S} = \delta^{33}\text{S} - 1000 \times$
19 1022 $[(\delta^{34}\text{S}/1000 + 1)0.515 - 1]$. Compositional field of shergottites and weighted mean used as
20 1023 revised estimate for the juvenile Martian sulfur composition after Franz et al. (2019),
21 1024 excluding the samples that were described as contaminated by crustal materials. Note the overall
22 1025 negative $\delta^{34}\text{S}$ values of NWA 7533 sulfides for slightly negative $\Delta^{33}\text{S}$ values compared to
23 1026 shergottites. Typical error bars on shergottite data display 2σ uncertainties.

24
25
26
27
28
29 1027
30 1028 Figure 3 : $\delta^{34}\text{S}$ vs. Ni and $\Delta^{33}\text{S}$ vs. Ni diagrams for NWA 7533 pyrite (NWA7533-5) (SEM
31 1029 analyses for Ni).

32
33
34
35
36
37 1030
38 1031 Figure 4 : $\Delta^{33}\text{S}$ vs. $\Delta^{36}\text{S}$ diagrams for NWA 7533 sulfides. $\Delta^{36}\text{S} = \delta^{36}\text{S} - 1000 \times$
39 1032 $[(\delta^{34}\text{S}/1000 + 1)1.9 - 1]$. Data for SNC meteorites from Franz et al., (2014, 2019).

40 1033
41 1034 Figure 5. Time-resolved LA-ICPMS spectra collected along the laser traverse through a Fe
42 1035 oxyhydroxide pseudomorph replacing pyrite.

43 1036
44 1037 Figure 6 : Se vs. S plots for NWA 7533. Color symbols correspond to the rastered LA-ICPMS
45 1038 analyses of the different lithological components of NWA 7533 (Humayun et al., 2013). NWA
46 1039 pyrite and Fe oxyhydroxide compositions from Lorand et al (2018b). The blue arrow depicts the
47 1040 preferential leaching of S with respect to Se resulting from terrestrial weathering. Putative
48 1041 composition of martian sulfates after Wang and Becker (2017).

1042

1043 Figure 7. Comparison of NWA 7533 pyrite compositions with SNC meteorites in a $\delta^{34}\text{S}$ vs $\Delta^{33}\text{S}$
1044 diagram. A = ALH 84001; L = Lafayette; N = Nakhla; Y = Y000593 (nakhlite); M = Miller
1045 Range nakhlites; NWA 998 and NWA 6148 : nakhlites; WSS : water-soluble sulfates; AVS :
1046 acid-volatile sulfides; CRS : Chromium-reducible sulfides; Py : pyrite. Other data : bulk-rock
1047 analyses. Note the overall negative $\delta^{34}\text{S}$ values of NWA 7533 sulfides for slightly negative $\Delta^{33}\text{S}$
1048 values compared to nakhlite sulfates. Arrow materializes possible thermochemical reduction of
1049 sulfates into NWA 7533 hydrothermal sulfides.

1050

1
2
3
4
5
6
7
8
9
10
11
12
13
14
15
16
17
18
19
20
21
22
23
24
25
26
27
28
29
30
31
32
33
34
35
36
37
38
39
40
41
42
43
44
45
46
47
48
49
50
51
52
53
54
55
56
57
58
59
60

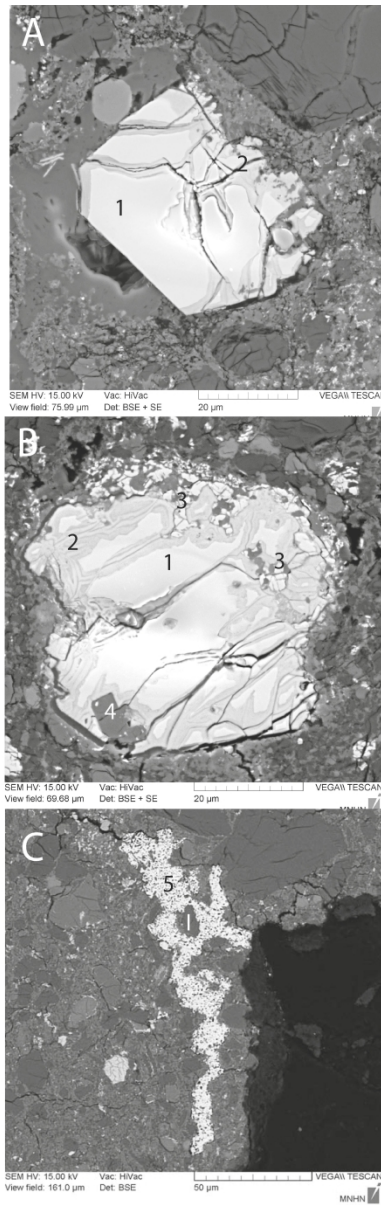


Fig. 1

210x297mm (600 x 600 DPI)

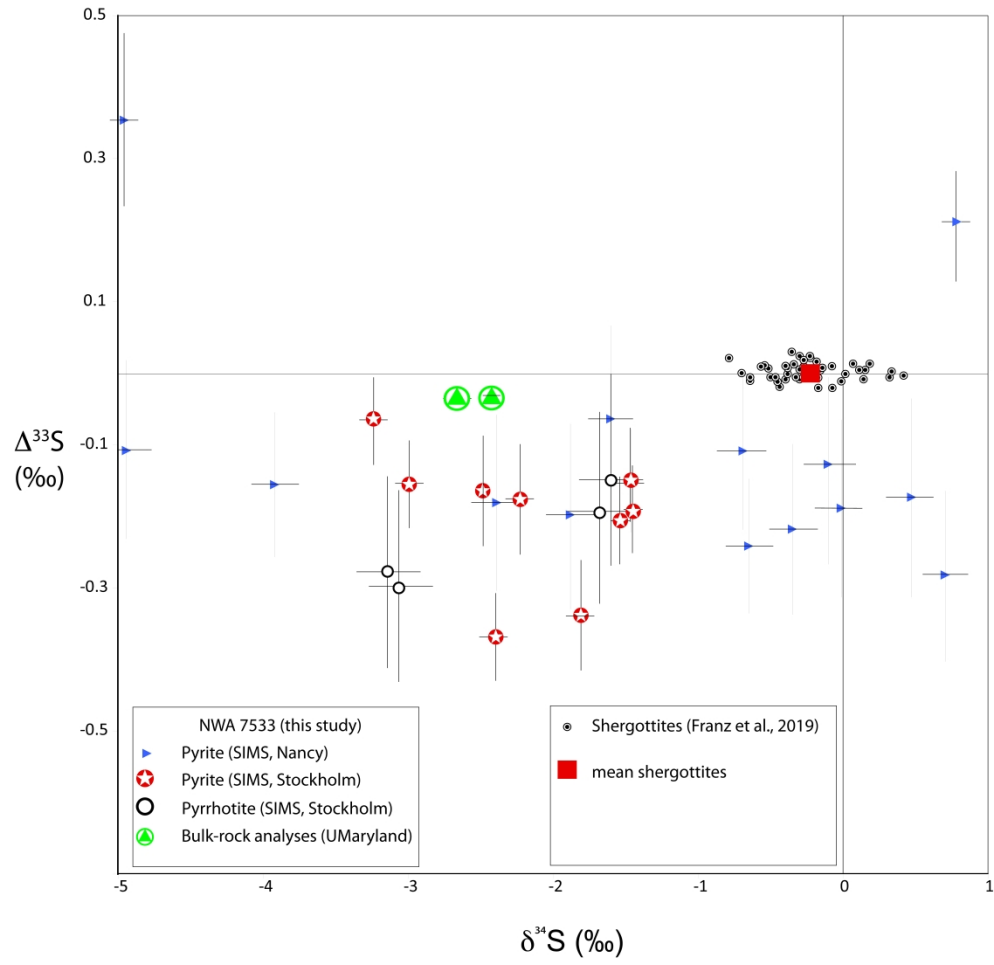


Fig. 2

698x855mm (600 x 600 DPI)

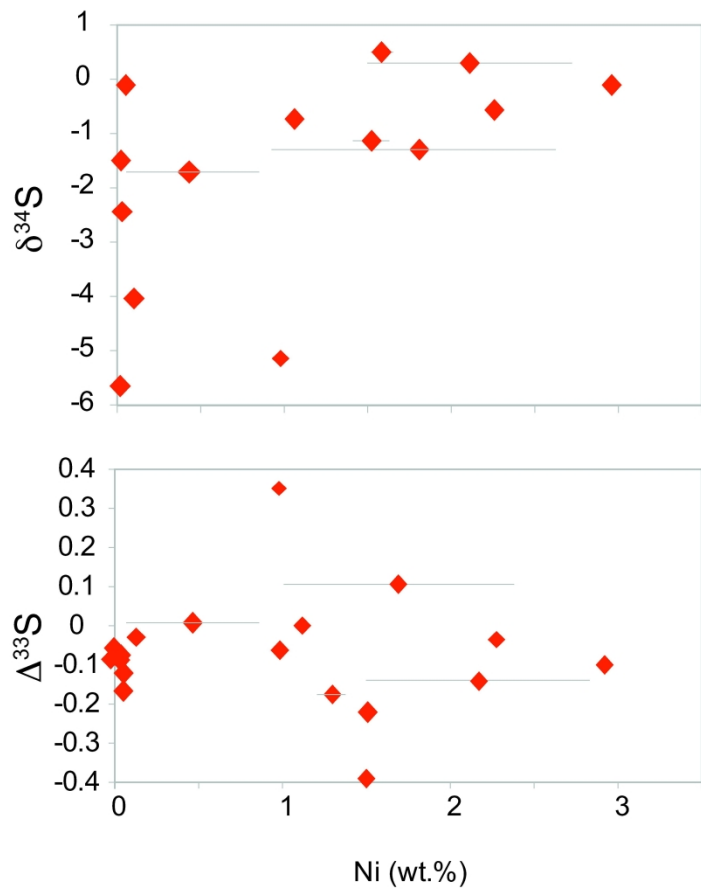


Fig. 3

228x231mm (600 x 600 DPI)

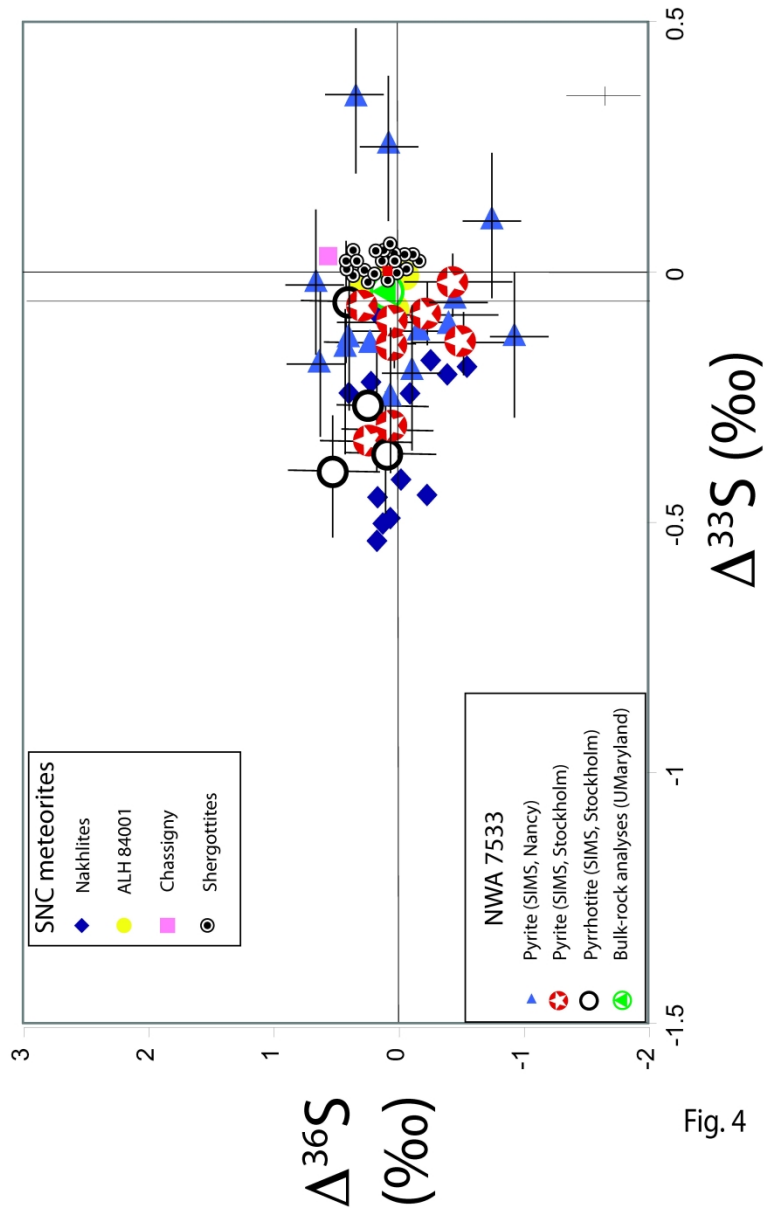


Fig. 4

188x295mm (600 x 600 DPI)

1
2
3
4
5
6
7
8
9
10
11
12
13
14
15
16
17
18
19
20
21
22
23
24
25
26
27
28
29
30
31
32
33
34
35
36
37
38
39
40
41
42
43
44
45
46
47
48
49
50
51
52
53
54
55
56
57
58
59
60

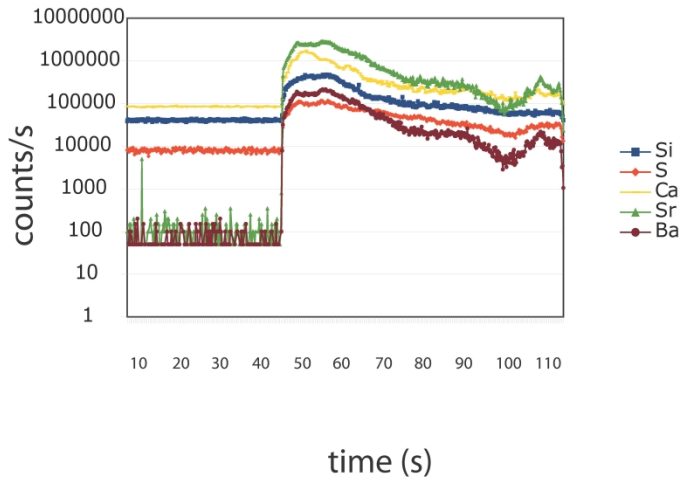


Fig. 6

210x297mm (600 x 600 DPI)

1
2
3
4
5
6
7
8
9
10
11
12
13
14
15
16
17
18
19
20
21
22
23
24
25
26
27
28
29
30
31
32
33
34
35
36
37
38
39
40
41
42
43
44
45
46
47
48
49
50
51
52
53
54
55
56
57
58
59
60

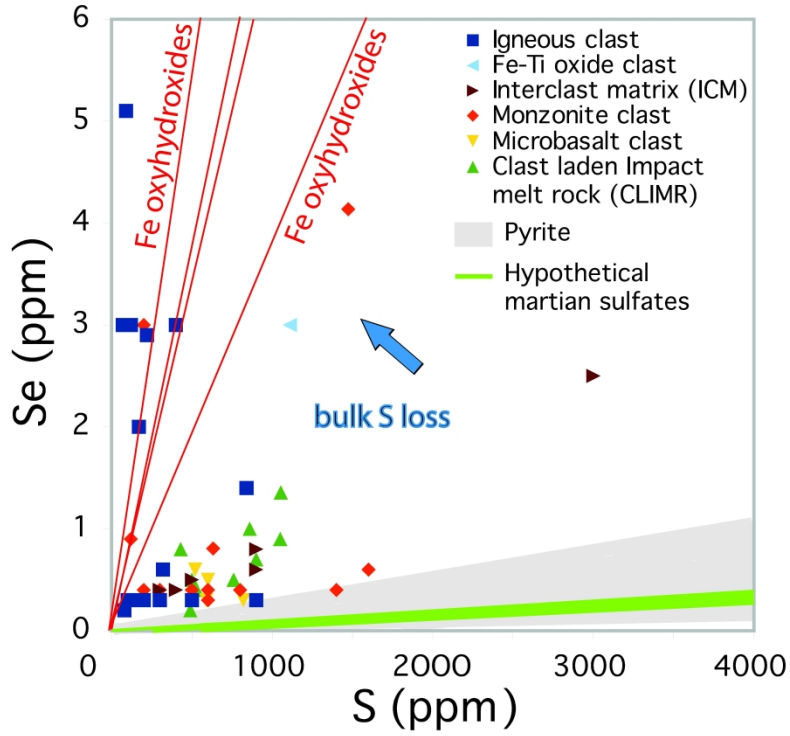
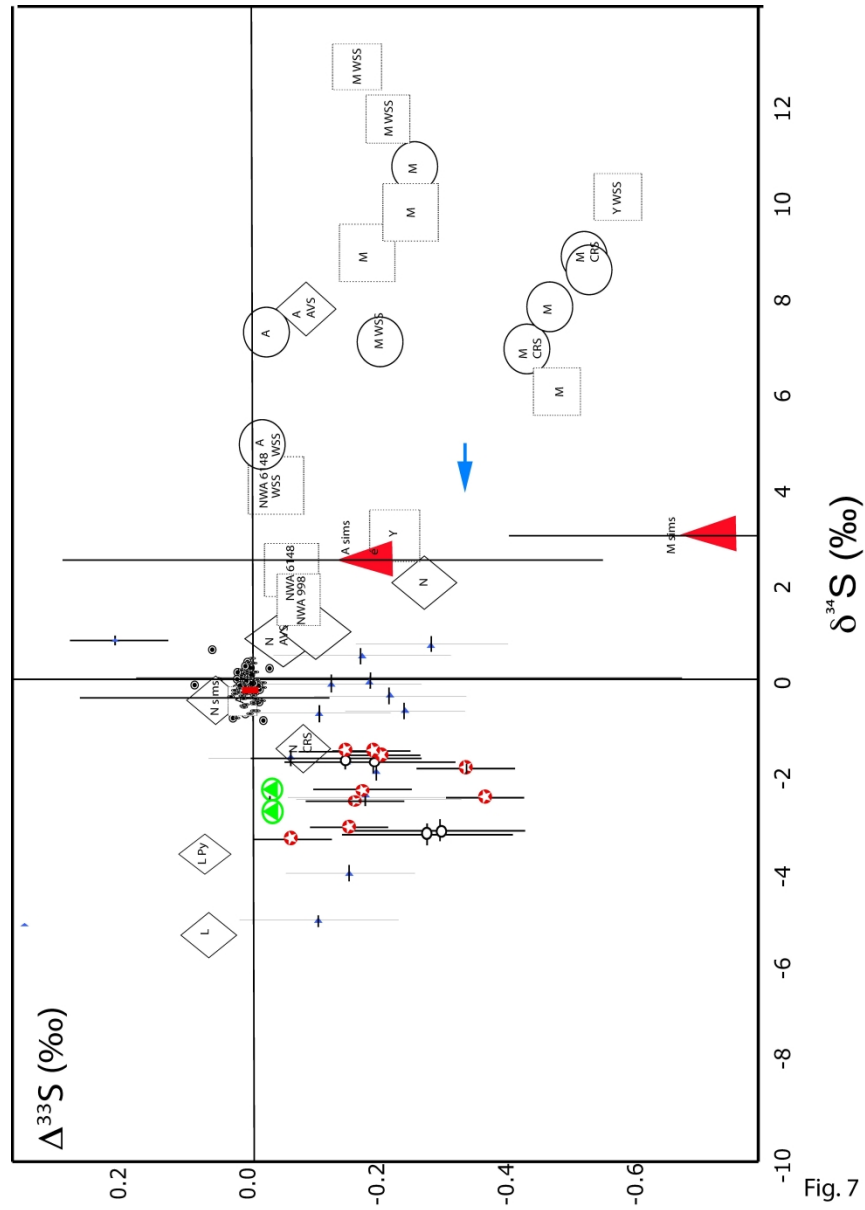


Fig. 5

233x252mm (600 x 600 DPI)



211x296mm (600 x 600 DPI)

Table 1. S isotopic compositions of sulfides in NWA 7533 (Canon Diablo-normalized)

	S (ppm)	$\delta^{34}\text{S}$ (‰)	2σ	$\Delta^{33}\text{S}$ (‰)	2σ	$\Delta^{36}\text{S}$ (‰)	2σ
Bulk-rock (U Maryland)							
BB-UMD-1	920	-2.39	0.013	-0.026	0.012	0.002	0.105
BB-UMD-2	805	-2.673	0.027	-0.031	0.01	0.001	0.076
average	863	-2.532	0.015	-0.029	0.010	0.002	0.09
NWA 7533-4 (NORDSIMS)							
Site 8a Pyrite		-1.82	0.23	-0.34	0.17	0.08	0.53
Site 8b Pyrite		-2.5	0.23	-0.36	0.18	0.12	0.66
Site 5b Pyrite		-1.54	0.18	-0.21	0.12	0.03	0.44
Site 15 Pyrite		-2.5	0.17	-0.12	0.14	0.49	0.51
Site 16a Pyrite		-1.63	0.17	-0.21	0.14	-0.55	0.53
Site 16b Pyrite		-3.25	0.17	-0.05	0.14	-0.43	0.49
Site 17 Pyrite		-2.99	0.18	-0.16	0.13	-0.004	0.45
Site b1a Pyrite		-2.22	0.19	-0.16	0.16	-0.083	0.54
Site b1b Pyrite		-1.5	0.17	-0.13	0.14	-0.39	0.53
Site 9a Pyrrhotite		-1.65	0.38	-0.19	0.28	0.12	0.81
Site 9b Pyrrhotite		-1.61	0.41	-0.14	0.28	0.39	0.71
Site 11 Pyrrhotite		-3.16	0.4	-0.26	0.3	0.05	0.6
Site 12 Pyrrhotite		-3.11	0.32	-0.28	0.23	0.49	0.67
average		-2.22		-0.186		0.01	
2SD		1.38		0.18		0.66	
wtd. Av. (95% conf.)		0.41		0.044		0.20	
MSWD		42.		1.11		1.4	
NWA 7533-5 (Nancy).							
Site A Pyrite		-1.71	0.32	-0.01	0.18	0.59	0.48
Site 8 Pyrite		0.6	0.32	-0.22	0.18	0.03	0.48
Site -1a Pyrite		-0.44	0.32	-0.17	0.18	0.57	0.48
Site -1b Pyrite		-2.49	0.32	-0.12	0.18	0.3	0.48
Site -17 Pyrite		-0.11	0.32	-0.12	0.18	0.15	0.48
Site -19 Pyrite		0.39	0.32	-0.13	0.18	0.37	0.48
Site -12 Pyrite		-0.79	0.32	-0.04	0.18	-0.49	0.48
Site -C Pyrite		-4.02	0.32	-0.1	0.18	-0.21	0.48
Site -6-1 Pyrite		-1.33	0.32	0.11	0.18	-0.74	0.48
Site 6-2 Pyrite		-0.75	0.32	-0.18	0.18	-0.15	0.48
Site -B1 Pyrite		-1.21	0.32	-0.38	0.18	-2.27	0.48
Site G Pyrite		-5.08	0.32	-0.08	0.18	-2.22	0.48
Site -F-1 Pyrite		-1.57	0.32	-0.09	0.18	-0.4	0.48

1						
2						
3	Site -F-2 Pyrite	-0.19	0.32	-0.11	0.18	-0.92 0.48
4	Site F-4 Pyrite	-5.58	0.32	0.35	0.18	0.26 0.48
5	Site 16-1 Pyrite	-2.01	0.32	0.24	0.18	0.02 0.48
6						
7	average*	-1.65		-0.12		0.32
8	2SD	3.69		1.5		1.74
9	wtd. av. (95% conf.)	0.98		0.064		0.46
10	MSWD	132		1.5		13.0
11						

12
13 * : exclude the positive values of $\Delta 33S$ in Site F-4 Pyrite and Site 16-1 Pyrite

14
15 2SD is the simple 2x standard deviation on the values (measures variation in a data set regard
16 wtd.av. is the weighted average uncertainty on the data along its MSWD value (measures the
17
18
19
20
21
22
23
24
25
26
27
28
29
30
31
32
33
34
35
36
37
38
39
40
41
42
43
44
45
46
47
48
49
50
51
52
53
54
55
56
57
58
59
60

1
2
3
4
5
6
7
8
9
10
11
12
13
14
15
16
17
18
19
20
21
22
23
24
25
26
27
28
29
30
31
32
33
34
35
36
37
38
39
40
41
42
43
44
45
46
47
48
49
50
51
52
53
54
55
56
57
58
59
60

For Peer Review Only

1
2
3
4
5
6
7
8
9
10
11
12
13
14
15 less of individual run uncertainties);)
16 σ spread)
17
18
19
20
21
22
23
24
25
26
27
28
29
30
31
32
33
34
35
36
37
38
39
40
41
42
43
44
45
46
47
48
49
50
51
52
53
54
55
56
57
58
59
60

For Peer Review Only

1
2
3
4
5
6
7
8
9
10
11
12
13
14
15
16
17
18
19
20
21
22
23
24
25
26
27
28
29
30
31
32
33
34
35
36
37
38
39
40
41
42
43
44
45
46
47
48
49
50
51
52
53
54
55
56
57
58
59
60

For Peer Review Only

Table 2. Laser Ablation inductively-coupled mass spectrometry (LA-ICPMS) analyses of pyrite alteration products.

Fe oxyhydroxides (pyrite alteration products)

	1	2	3	4	5	6	EMPA (n=15)*
	LA- ICPMS	LA- ICPMS	LA- ICPMS	LA- ICPMS	LA- ICPMS	LA- ICPMS	
S (ppm)	2392	2059	3061	4128	3728	2299	2400 +/-130
Ca	4455.5	13158.6	10681.2	5349.9	11609.4	8009.6	9500 +/-201
Sr	79.5	75.6	372.3	386.2	411.3	283.4	
Ba	227.1	91.1	198.2	283.6	271.6	233.6	
detection limits							
S (ppm)	2.83	3.09	4.48	4.14	7.76	3.77	
Ca	3.68	4.17	6.20	5.82	11.20	5.81	
Sr	0.001	0.001	0.002	0.002	0.004	0.002	
Ba	0.009	0.009	0.014	0.013	0.027	0.014	
	0.003	0.003	0.005	0.005	0.010	0.004	
Apatite							
	1	4	6	7	8	9	10
	LA- ICPMS	LA- ICPMS	LA- ICPMS	LA- ICPMS	LA- ICPMS	LA- ICPMS	LA- ICPMS
S (ppm)	229.9	230.2	209.3	217.2	229.6	231.1	267.6
Ca	IS	IS	IS	IS	IS	IS	IS
Sr	137.3	157.6	145.6	112.7	179.9	197.7	143.9
Ba	6.73	8.98	8.05	5.09	7.28	12.4	5.13
detection limits							
S (ppm)	2.01	2.81	2.40	3.37	3.10	3.42	3.87
Sr	0.001	0.001	0.001	0.001	0.009	0.001	0.001
Ba	0.006	0.009	0.007	0.009	0.008	0.009	0.011

*Electron Microprobe analyses-EMPA (Lorand et al., 2015) ; IS = Internal Standard.